Journal of Structural Geology 184 (2024) 105153

Contents lists available at ScienceDirect

Journal of Structural Geology

journal homepage: www.elsevier.com/locate/jsg

Boudinage and folding of oblique single layers in bulk constrictional strain fields: Results from analogue modelling

Chao Cheng [a,*], Janet Zulauf [a], Gernold Zulauf [a], Elke Hattingen [b]

[a] Institut für Geowissenschaften, Goethe-Universität Frankfurt am Main, Altenhöferallee 1, D-60438, Frankfurt am Main, Germany
[b] Institut für Neuroradiologie, Universitätsklinikum, Goethe-Universität Frankfurt am Main, Schleusenweg 2-15, D-60528, Frankfurt am Main, Germany

ARTICLE INFO

Keywords:
Coeval folding and boudinage
Non-cylindrical folds
Dome-and-basin structure
Constriction
Deformation oblique layer
Analogue modelling

ABSTRACT

We conducted scaled analogue modelling to show the influence of varying single layer initial orientation on the geometry of folds and boudins in a bulk constrictional strain field. The initial angle between the plane of shortening and the competent layer ($\theta_{Z(i)}$) was incrementally increased from 0° to 90° by multiples of 11.25°. While the amount of layer thickening decreased with increasing $\theta_{Z(i)}$, the deformation structures produced range from pure dome-and-basin folds to coeval folds and boudins. Based on the attitude of fold axes, there are extension-parallel (F_{EPR}) and extension-perpendicular (F_{EPP}) folds, with axes subparallel and subperpendicular to the principal stretching axis (X), respectively. Coeval growth of F_{EPR} folds and boudins occurred when $\theta_{Z(i)} >$ ca. 25°. The F_{EPP} folds can be subdivided into a first type which affect the entire layer (if $\theta_{Z(i)}$ ranges between 11.25 and 78.75°) and a second type, referred to as FB_{EPP} folds, which are affecting pre-existing boudins if $\theta_{Z(i)} > 45°$. The interlimb angle of all types of folds increases with increasing $\theta_{Z(i)}$. Folds and boudins similar to the ones produced in this study can be found in salt domes and in tectonites of subduction zones.

1. Introduction

As widespread deformation structures in naturally layered rocks, folds and boudins occur across the whole range of structural levels and spatial scales within various geotectonic regimes (e.g. Ramberg, 1955; Rast, 1956; Smith, 1977; Hudleston and Lan, 1993; Marques and Cobbold, 1995; Goscombe and Passchier, 2003; Druguet et al., 2009; Hudleston and Treagus, 2010; Marques et al., 2010, 2012; Reber et al., 2010; Arango et al., 2013; Schmalholz and Mancktelow, 2016; Mukherjee, 2020; Alsop et al., 2021; Zawaski et al., 2020; Nabavi and Fossen, 2021; Papeschi et al., 2022). These structures play an important role to estimate and reconstruct the rheological properties and kinematic conditions associated with the deformation. Buckling and necking, one of the most important mechanisms inducing folds and boudins, respectively, are the two types of preferred deformation patterns of rheologically stratified rocks. This preference arises because bucking and necking minimize the corresponding mechanical work that is required to extend or shorten the layers (Schmalholz and Mancktelow, 2016; Zulauf et al., 2020b). Buckle folds and boudins are closely related to each other in some respects. First of all, both structures can be formed under the same fundamental driving mechanism of the difference in strain rate between the competent layer and the incompetent matrix of the stratified rocks (Ramberg, 1959). Secondly, both can be formed under the conditions related to structural softening (Schmalholz and Mancktelow, 2016). Thirdly, both buckle folds and boudins can be formed under an identical frame of mechanical instability based on the hydrodynamic stability theory for power-law materials, thus exhibiting the same dominant wavelength (Zulauf et al., 2020b). If the viscosity ratio and the power-law stress exponent of layer and matrix increase, the amplification rates also increase (Fletcher, 1974; Smith, 1975, 1977). However, in contrast to folding, boudinage is not recoverable (Sengupta, 1983). Compared to boudinage, folding exhibits a greater amplification rate and a higher degree of structural softening (Schmalholz and Mancktelow, 2016). Folding is applicable to both linear and power-law viscous rheology, while necking and related boudinage are restricted to the latter (Fletcher, 1974; Smith, 1977, 1979).

Flinn (1962) carried out theoretical studies of folding and boudinage in three-dimensional strain fields: (1) constrictional strain ($1 < k < \infty$), (2) flattening strain ($0 < k < 1$), and (3) plane strain ($k = 1$), where k is the Flinn parameter (Fig. 1 in Flinn, 1962). Exhaustive research regarding folds and boudins developing under bulk coaxial plane strain has been conducted in the last decades (e.g. Zulauf et al., 2020a, 2020b,

* Corresponding author.
E-mail address: c.cheng@em.uni-frankfurt.de (C. Cheng).

https://doi.org/10.1016/j.jsg.2024.105153
Received 21 January 2024; Received in revised form 26 April 2024; Accepted 8 May 2024
Available online 11 May 2024

2021). Cylindrical folds and boudins will grow if the layer is oriented perpendicular to the principal stretching axis (*X*) or to the principal shortening axis (*Z*), respectively (Marques et al., 2012; Zulauf et al., 2020b). Under these conditions, the axes of both folds and boudins are subparallel to the intermediate strain axis (*Y*) (e.g. Ramberg, 1955; Hudleston, 1973; Schöpfer and Zulauf, 2002; Zulauf et al., 2003; Schmalholz, 2006b; Schmalholz et al., 2008; Hudleston and Treagus, 2010; Reber et al., 2010; Adamuszek et al., 2011; Abe and Urai, 2012; Zulauf et al., 2020b). Boudins and folds can grow simultaneously if the competent layer is oriented perpendicular to the intermediate *Y*-axis under bulk coaxial plane strain (Grujic and Mancktelow, 1995). Under these conditions, the axes of torn boudins and extension-parallel folds are parallel to the *Z*- and *X*-axis, respectively (Zulauf et al., 2003; Enama Mengong and Zulauf, 2006).

In cases of an oblique competent layer, with a general non-orthogonal orientation to the principal strain axes under bulk coaxial plane strain, the situation becomes more complex as the layer rotates during progressive deformation. When the oblique layer is aligned parallel to the *Y*-axis, it rotates slower than a corresponding passive plane (Price, 1967; Zulauf et al., 2020a). However, when the oblique layer is aligned parallel to the *X*- or *Z*-axis, its rotation rate is nearly the same as that of a passive plane (Zulauf et al., 2020b, 2021). The orientation and rotation of the layer can also affect the geometric parameters of coeval folds and boudins. When the competent layer is initially aligned parallel to the *Y*-axis and oblique to the *X*- and *Z*-axis, asymmetric folds (Price, 1967; Treagus, 1973; Anthony and Wickham, 1978; Zulauf et al., 2020a) and asymmetric boudins (e.g. Abe and Urai, 2012) will develop under coaxial plane strain. Coeval development of extension-parallel folds and boudins is feasible under coaxial plane strain, if the layer is initially parallel to the *X*-axis, but oblique to the *Y*- and *Z*-axis (Zulauf et al., 2020b). The same holds for cases where the competent layer is initially parallel to the *Z*-axis, but is oblique to the *X*- and *Y*-axis, and the initial angle between layer and *X*-axis is $< 45°$. Competent layers inclined to the *X*-axis at an angle $>45°$ will be converted into periclinal folds (Zulauf et al., 2021).

Thus, non-cylindrical folds and boudins can grow within oblique competent layers, although the deformation is plane and coaxial. Such non-cylindrical structures, on the other hand, can develop in non-oblique competent single layers if the bulk strain is not plane, i.e. pure and general constriction or pure and general flattening (Treagus and Treagus, 1981; Weijermars, 1997; Kobberger and Zulauf, 1995; Zulauf et al., 2003, 2011, 2016; Zulauf and Zulauf, 2005). Moreover, based on the results of previous physical and numerical experiments mentioned above, coeval folding and boudinage are possible if an oblique or non-oblique competent layer is deformed under bulk coaxial plane strain, or if the competent layer has a general orthogonal orientation with respect to the principal strain axes in non-plane deformation settings. Physical and numerical experiments focusing on non-plane coaxial deformation of oblique single (and multi) layers, however, are entirely lacking, and the structures related to these conditions are largely unknown. As flattening and constrictional finite strain are frequent in nature, and the number of 3D folds and boudins described from natural tectonites increases, such experiments are essential.

The present study concentrates on the growth of folds and boudins in initially oblique single layers during coaxial bulk constriction. Scaled analogue modelling was applied to investigate the effect of initial layer inclination on the geometrical parameters of folds and boudins. We conducted a sequence of experiments with varying initial angle between the competent layer and the shortening axis, while all the other parameters, such as layer thickness or viscosity ratio between layer and matrix did not change. The results of these experiments will be described and discussed. Finally, examples of natural coeval folds and boudins will be presented that might be attributed to the deformation of oblique single layers under bulk constriction.

2. Methods

2.1. Analogue material and experimental parameters

For the experiments, we used plasticine and modified plasticine as rock analogue materials, which display strain-rate softening features with effective viscosity decreasing with increasing strain rate. For further details regarding the properties of plasticine and its application as a rock analogue, see Zulauf and Zulauf (2004).

Two different types of plasticine with the viscosity ratio of $m = 18$ were used for the competent layer and incompetent matrix, which are the Kolb brown/Stange weiß type with higher viscosity ($\eta_{Layer} = 4.0 \times 10^9$ Pa s) and stress exponent ($n_{Layer} = 6$) and Beschuss-Knete type with lower viscosity ($\eta_{Matrix} = 2.2 \times 10^8$ Pa s) and stress exponent ($n_{Matrix} = 4$), respectively (Table S1, Supplement). The viscosities mentioned above are related to the strain rate of $\dot{e} = 1.9 \times 10^{-5}$ s^{-1} with finite constrictional strain $e_Z = e_Y = -50\%$. It is suggested that the typical

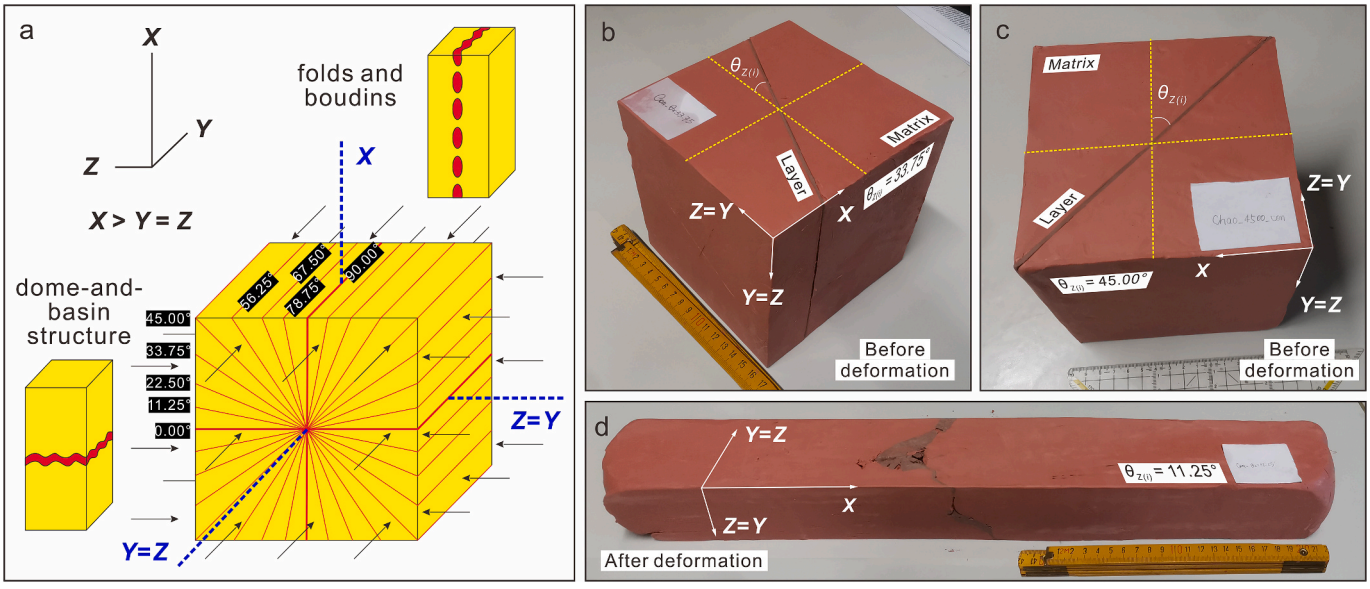

Fig. 1. (a) Experimental setup of folding and boudinage of an oblique competent layer under bulk coaxial constriction. (b) Photograph of undeformed sample when $\theta_{Z(i)}$ was set at 33.75°. (c) Photograph of undeformed sample when $\theta_{Z(i)}$ was set at 45.00°. (d) Deformed sample when $\theta_{Z(i)}$ was set at 11.25°.

stress exponent of coarse-grained rocks subjected to dislocation creep is between 3 and 5, but as high as 8 has also been proposed (see Zulauf et al., 2023 and references therein)

Nine experimental runs were conducted in bulk constrictional strain fields, each with a different initial angle between the competent layer and the *Z*-axis ($\theta_{Z(i)}$, Fig. 1). The initial orientation of the pre-deformation layer was incrementally changed by multiples of 11.25° (Fig. 1a), starting from the *YZ*-plane ($\theta_{Z(i)} = 0°$, dome-and-basin folding) until the *XY*=*Z*-plane ($\theta_{Z(i)} = 90°$, coeval folding and boudinage) was attained. We set the rock analogues as a standard cube with a side length of 15 cm. The layer has been set with an initial thickness (H_i) of 1.5 ± 0.1 mm and embedded within the weaker matrix (Fig. 1b and c). Experimental procedures were conducted at a constant temperature T = 25 °C (Table S1, Supplement).

In laboratory modeling of rock deformation, the model serves as a small-scale geometric replica of the natural rocks and deforms at higher strain rates, allowing body forces such as gravity as well as inertia to be neglected (Zulauf et al., 2020b). To simulate deformation structures of natural rocks, the models in the experiments are properly scaled concerning the geometric, kinematic, and dynamic similarity of natural rocks (e.g. Hubbert, 1937; Ramberg, 1981; Weijermars and Schmeling, 1986). Notably, the experiments feature a substantially higher strain rate than typically found in naturally deformed rocks. Moreover, the models of the present experiments were not subjected to confining pressure, which practically occurs in nature. Nevertheless, dynamic similarity is provided between the non-linear viscous analogue materials and natural rocks. The models can be used to model folding of rocks where both layer and matrix are undergoing dislocation creep. Dislocation creep is common as deformation mechanism in most silicate phases if temperature is elevated at deeper structural levels (e.g. Carter and Tsenn, 1987).

Particular attention has to be paid to possible boundary effects of the physical experiments (e.g. Marques and Podladchikov, 2009; Marques and Mandal, 2016), especially for oblique layers, because the ends of the layer(s) tend to slide along the boundaries and parts of the layer can be pulled out of the sample (Zulauf et al., 2020a, 2023). Oblique loading of the ends introduces additional perturbation components because the planar boundary is no longer parallel to the axial plane of the developing folds (Schmalholz and Mancktelow, 2016). To reduce boundary effects due to friction between the specimen and the aluminium plates of the machine, the sides of the specimen were lubricated with vaseline. Moreover, to eliminate boundary effects, only the structures in the central part of the samples were considered during geometrical analyses, which are largely free from boundary effects.

2.2. Experimental apparatus and geometrical analysis

A three-dimensional coaxial deformation rig was used to deform the plasticine models as illustrated in Fig. 2. Details regarding the components, operation mechanism, and experimental procedure of the deformation apparatus are described by Zulauf et al. (2009).

To visualize the deformation style and detailed 3D geometry of the complex structures of coeval folds and boudins, all deformed samples were investigated using computed tomography (CT). The distinct density ratio between layer and matrix allows that deformation structures can be optimally visualized via CT. The CT analyses were performed in the Neuroradiologie Department of Frankfurt University Clinic, using a multislice spiral CT-scanner (Phillips Brilliance 6 CT). The following geometric parameters of folds and boudins have been determined (Table S1, Supplement): initial (H_i) and finite (H_f) layer thickness, amplitude (A), arc-length (L), wavelength (λ), interlimb angle (δ), number of folds (N_{fold}), number of boudins (N_{boudin}), width of boudins (W_{Boudin}), width of boudin necks (W_{Neck}), and degree of layer rotation ($\theta_{Z(RL)}$). More details about the conditions for CT analysis are described by Zulauf et al. (2021, 2023). Based on the CT data, the geometry of folds and boudins was obtained using the following software: *ImageJ/FiJi* (http://imagej.net/Fiji/Publications), *Meshlab* (Visual Computing Lab – ISTI – CNR, http://meshlab.sourceforge.net), and *Smoooth* (rt-mp Software Development, info@rt-mp.com).

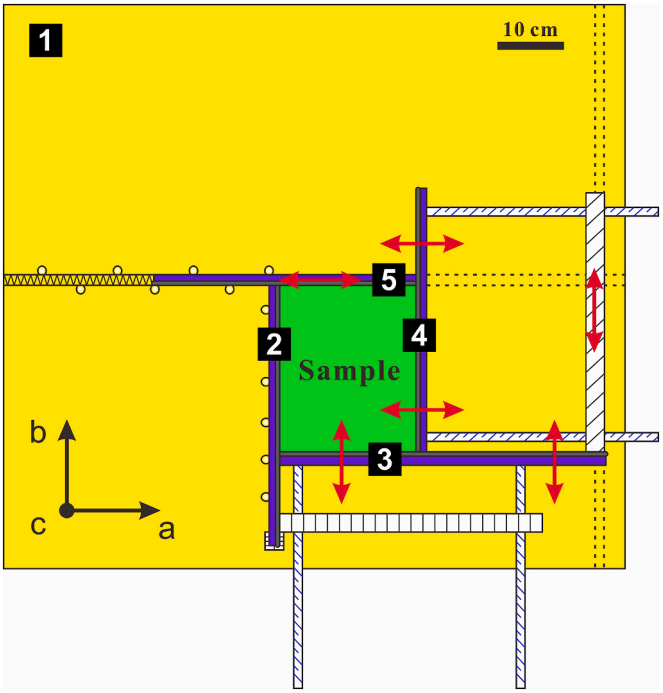

Fig. 2. Schematic drawing (top view) of the deformation apparatus used for the experiments (after Zulauf et al., 2003).

In addition, we analyzed two samples with non-cylindrical folds as digital 3D models using the software *MeshLab* and *Smoooth-ClassifyCurvature* to quantify the geometrical parameters of folds. The surface curvature as well as normal and tangent vectors were mathematically calculated using differential geometry (Mynatt et al., 2007). The fold classification is furthermore obtained based on the mean curvature and the Gaussian curvature. Different types of folded surfaces including domes, basins, antiformal saddles and synformal saddles can be identified using this software. The related methodology and workflow are delineated in detail by Zulauf et al. (2017). For the dome-and-basin structural sample of the present study, we gathered data sets from six different measuring profiles of each surface layer according to the following conditions: strongly kinked (*strK*) and slightly kinked (*sltK*) profiles, strongly curved (*strC*) and slightly curved (*sltC*) folds, distinct and relatively large domes and basins (*lrgDB*) and considering almost all possible profiles (*allP*). For the other sample, without a dome-and-basin structure, we obtained the data from several profiles of each surface layer which are approximately parallel to each other. Subsequently, the fold parameters, arc-length (L), wavelength (λ), orthogonal amplitude (A), and oblique amplitude (A') are quantified using the software.

3. Results

3.1. Geometry of folds and boudins

The geometrical parameters measured from the deformed single layers are listed in Table S1 (Supplement). The deformed layers are shown by CT models in Fig. 3. Column 3a displays the pre-deformational attitude of the competent layer. The views of column 3b are directed along the *X*-axis. The views in column 3c are directed perpendicular to the layer, with the exception of sample $\theta_{Z(i)} = 0°$. Extension-parallel folds (F_{EPR} folds), with their axis subparallel to the *X*-axis, and extension-perpendicular folds (F_{EPP} folds), with their axis perpendicular to the *X*-axis, are particularly well presented in oblique views of the

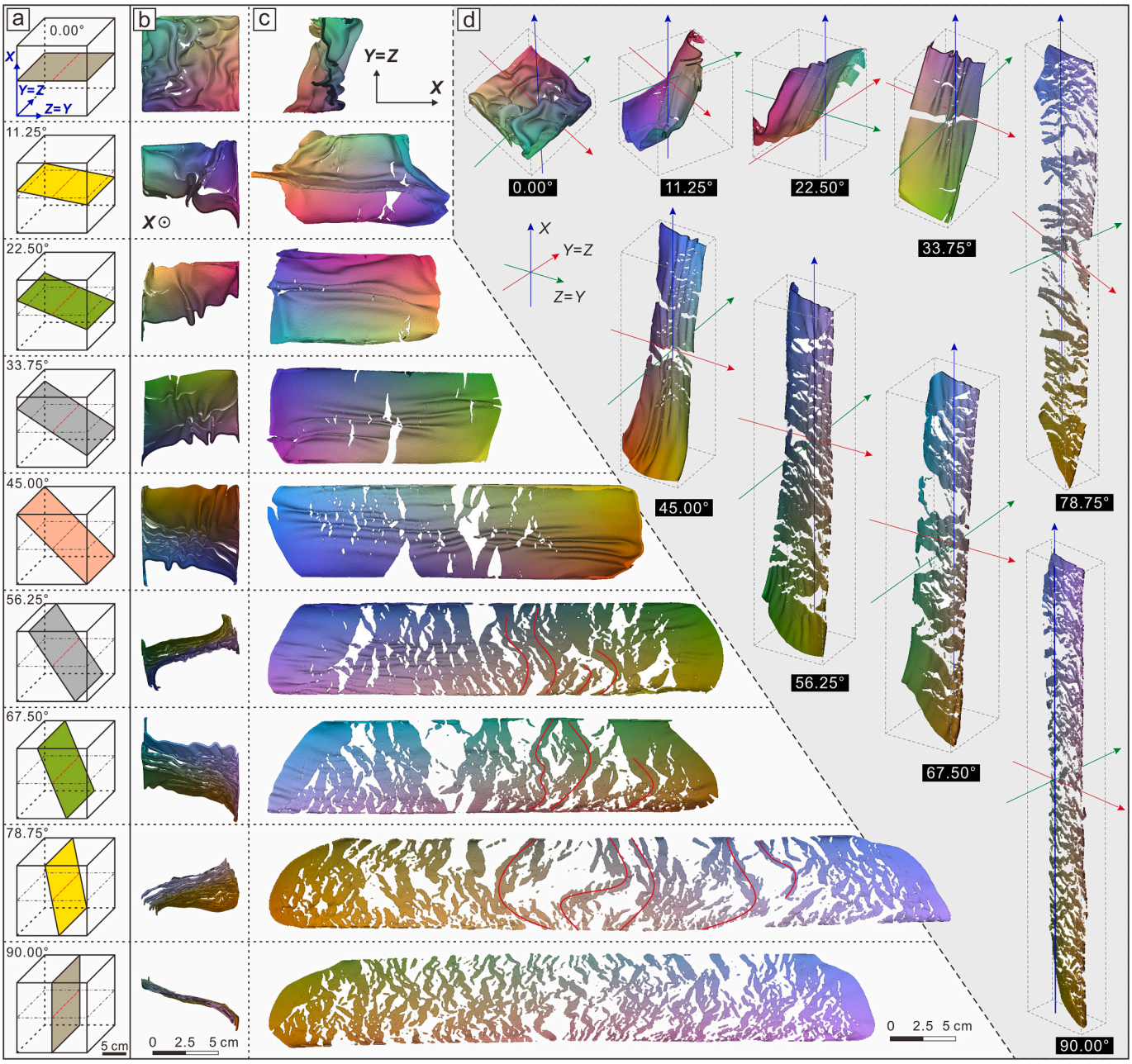

Fig. 3. 3D computer-tomographic images of the deformed competent layer of individual models. The incompetent matrix is neglected. (a) The cubes show the initial orientation of the layer $\theta_{Z(i)}$ with respect to the principal strain axes. (b) Views parallel to the *X*-axis. (c) Views perpendicular to the *XY*-plane and subperpendicular to the layer. Red lines indicate boudins affected by folding with the fold axes subperpendicular to the layer (FB_{EPP}). (d) Views oblique to the principal strain axes and to the deformed layer emphasizing the distinct geometry of folds and boudins. Note that $Y = Z$. (For interpretation of the references to color in this figure legend, the reader is referred to the Web version of this article.)

layer depicted in column 3d.

In the case that the original obliquity angle, $\theta_{Z(i)} = 0.00°$, the layer was oriented perpendicular to the *X*-axis (parallel to the *YZ*-plane, Fig. 1a and 3a). Radial shortening perpendicular to the *X*-axis produced dome-and-basin structures (Fig. 4), which were expected. Due to the fact that the layer in this particular instance was not oblique, it did not show significant rotation during deformation (ca. 5°, Fig. 5a). Nevertheless, significant layer thickening (ca. 77%) can be observed (Fig. 5b–Table S1, Supplement).

In consideration of the thickness factor of the deformed layer, we separated the upper and lower surface of the layer via *Meshlab* and analyzed them respectively to make a cross-check. The domes, basins, antifomal and synformal saddles of the selected areas have been distinguished with different colors (Fig. 4b–e). Subsequently, the separated main domes and basins of the model accompanied by their extremities and the extremity lines are produced using the software *Smoooth-AnalyzeModel* described above (Fig. 4c–f). As mentioned above, the geometrical data from six measuring profiles based on different criteria for each surface layer were obtained from this sample (Fig. 6, Table S2, Supplement).

There is no significant difference in the arc-length and wavelength between the different measuring profiles and between the upper and lower surface (Table S2, Supplement, Fig. 6a–c). The strongly curved profile shows the largest arc-length and the largest discrepancy between the arc-length and wavelength, which is reasonable. Overall, the mean values of arc-length and wavelength range from 24 to 28 mm and 19–21

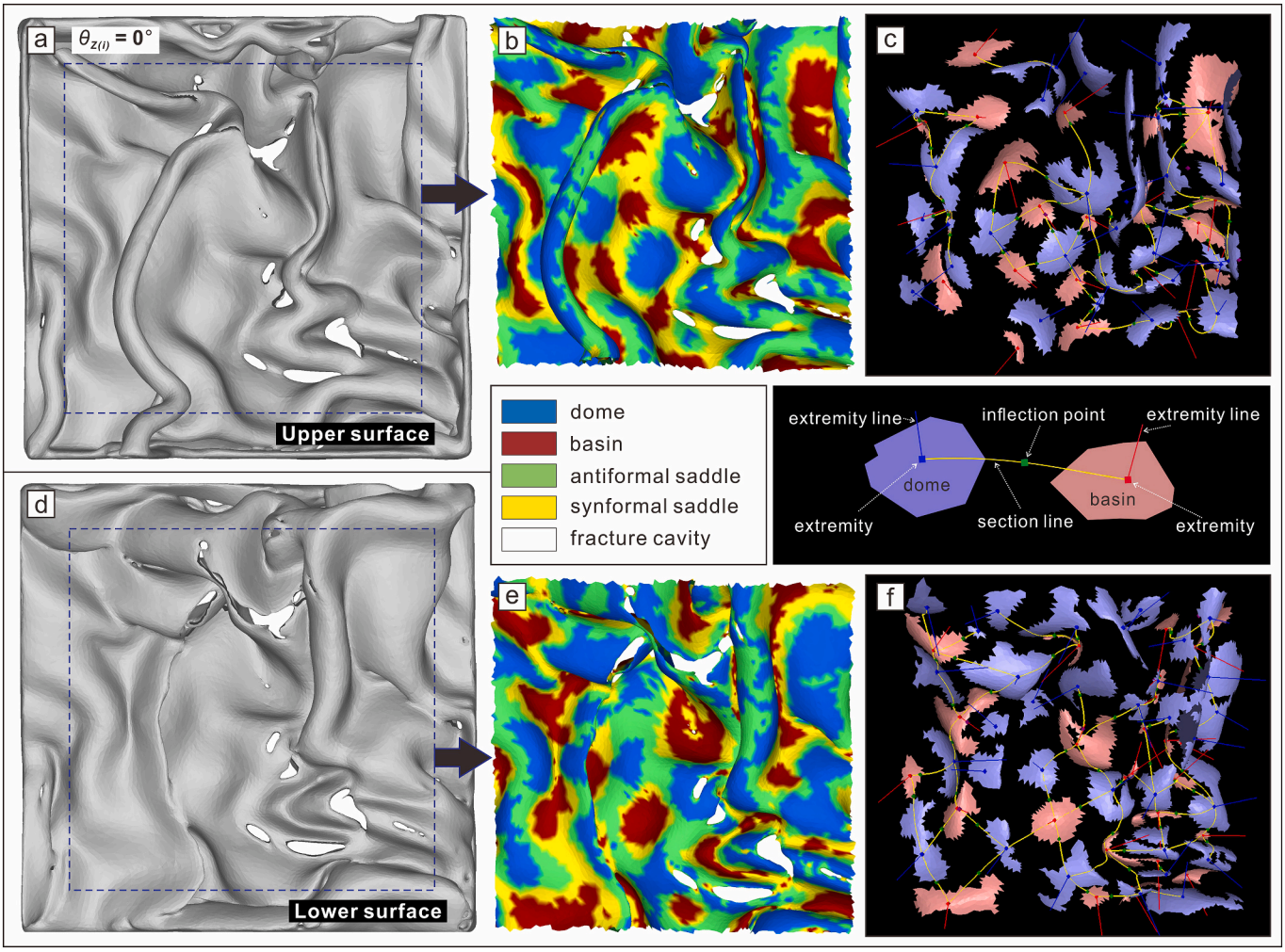

Fig. 4. 3D model of deformed competent layer affected by dome-and-basin structures when $\theta_{Z(i)} = 0°$. The model is based on a computer-tomographic analysis (for details of the experiments and measuring procedures, see Zulauf et al., 2016, 2017). The model is separated into the upper surface (a–c) and the lower surface (d–f) for a contrastive analysis. (a, d) Upper and lower surface of the model, which is constituted by numerous small polygons (triangles). Different grey levels result from different degrees of shading (inclination of the surface with respect to the light source). The dark blue dashed frame indicates the extent of detail for further 3D analyses. (b, e) Different fold types of the model depicting domes, basins, antiformal, and synformal saddles with different colors. (c, f) Separated domes (in blue) and basins (in pink) of the model. The extremities of domes and basins are shown by blue and red dots, respectively. The extremity lines of domes and basins are shown by blue and red lines, respectively. The yellow curved lines indicate selected measuring profiles. Inflection points are shown by green dots. (For interpretation of the references to color in this figure legend, the reader is referred to the Web version of this article.)

mm for the upper surface, and from 25 to 27 mm and 20–24 mm for the lower surface, respectively (Table S2, Supplement, Fig. 6a–c). The arc-length and wavelength from both surfaces yield mean values of 27 ± 10 mm and 21 ± 7 mm (Table S2, Supplement, Fig. 5c). The amplitudes are also similar on both surfaces. The mean values of the ortho amplitude range from 1.7 ± 1.1 mm to 3.6 ± 1.7 mm on the upper surface and from 2.1 ± 1.1 mm to 3.1 ± 1.7 mm on the lower surface (Table S2, Supplement, Fig. 6b–d), respectively. All these values from both surfaces yield a mean value of 2.8 ± 1.4 mm (Table S2, Supplement, Fig. 5e). The amplitudes obtained from the strongly curved profiles display higher values, while those obtained from the slightly curved profiles are much lower (Table S2, Supplement, Fig. 6b–d). The non-cylindrical folds developed an interlimb angle of ca. 70° with a large standard deviation (Table S1, Supplement, Fig. 5f).

In terms of the experiment with $\theta_{Z(i)} = 11.25°$, constriction along the *YZ*-plane led to the layer rotating towards the elongation direction (Fig. 1d and 3d). The layer was significantly rotated towards the *X*-axis during deformation ($e_Z = -50\%$) with a final orientation of ca. 49° with respect to the *Z*-axis (Fig. 5a). The angle of the rotated passive layer is slightly higher (ca. 58°, Fig. 5a). The magnitude of layer thickening is ca. 45% and thus much lower than in the previous run (Fig. 5b). Apart from the difference of layer thickening, the fold geometry is considerably different from the dome-and-basin structures described above. There are only a few slightly non-cylindrical tight to isoclinal F_{EPR} folds with axes oriented with small angle to the *X*-axis and open F_{EPP} folds with axes perpendicular to the *X*-axis (Fig. 3). The amplitude, arc- and wavelength of the F_{EPR} folds are similar to those of the dome-and-basin structures described above (Fig. 5c–e). Those of the F_{EPP} folds, however, are larger. The mean value of the amplitude of F_{EPP} folds is 4.5 mm (Fig. 5e), and the arc- and wavelength are ca. 44 and 34 mm, respectively. The interlimb angle (ca. 103°) of the F_{EPP} folds is also much higher than that of the F_{EPR} folds (Fig. 5f). Some of the hinges of the F_{EPR} folds are broken (Fig. 3). The tight to isoclinal F_{EPR} folds with large arc-length and amplitude as well as the open F_{EPP} folds with low amplitude develop with axes, which are perpendicular to each other (Fig. 3d).

When the value of $\theta_{Z(i)}$ was set to at 22.50°, the layer rotation towards the *X*-axis was slightly higher than in the previous run (ca. 55° respect to *Z*-axis, Fig. 5a). The thickening of the layer decreased to 34% (Fig. 5b). There are tight F_{EPR} folds, which show a tendency to periclines because of additional open F_{EPP} folds (Figs. 3 and 7a,e). The antiforms of

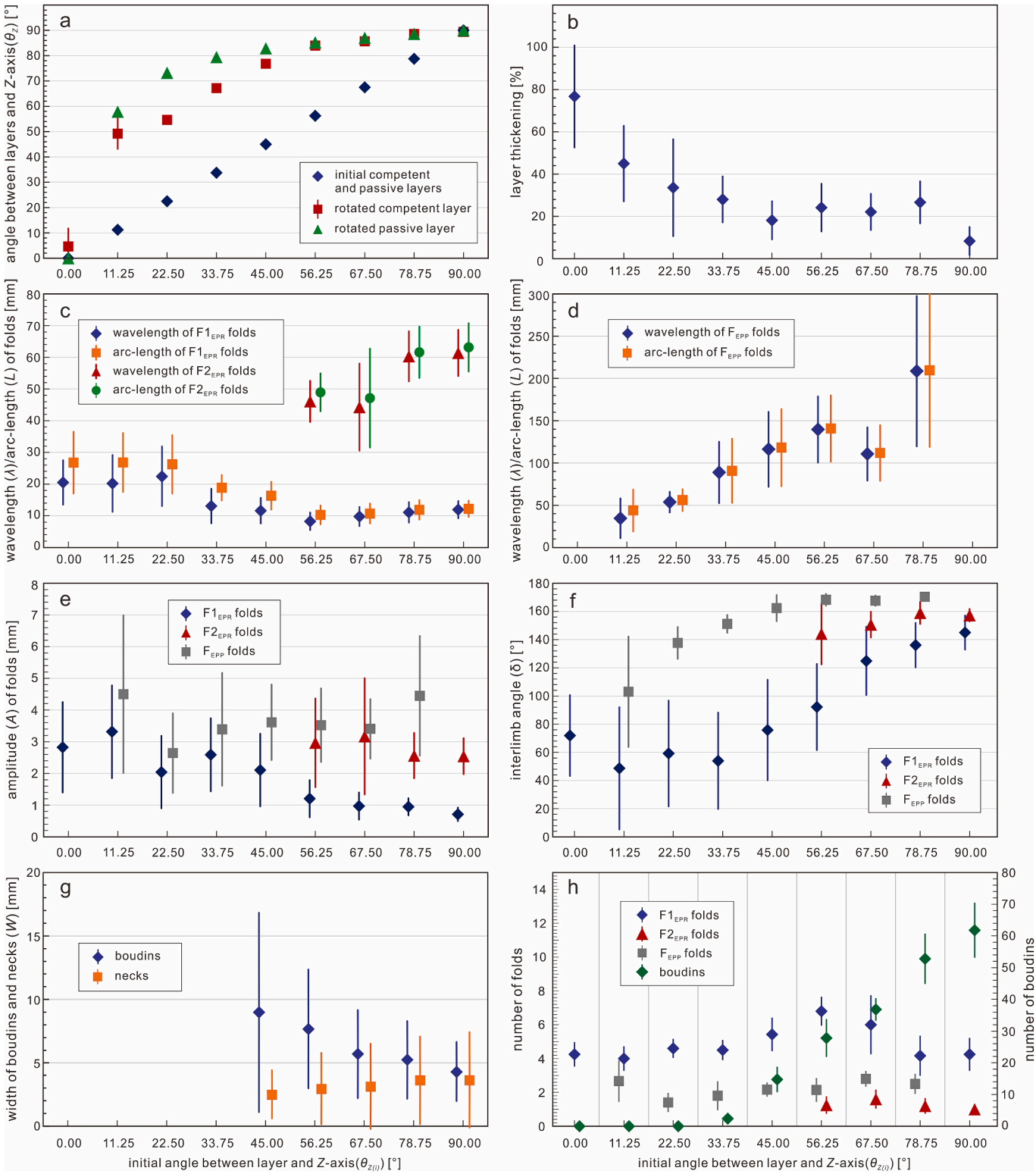

Fig. 5. Plots showing the relation between the initial orientation of layer ($\theta_{Z(i)}$) and the geometrical parameters of deformation structures: (a) finite angle between the competent/passive layer and the *Z*-axis; dark blue dots along the straight diagonal line indicate the initial attitude of the layer; (b) degree of layer thickening; (c) arc-length and wavelength of F_{EPR} folds; (d) arc-length and wavelength of the F_{EPP} folds; (e) amplitude of the folds; (f) interlimb angle of folds; (g) width of boudins and necks; (h) number of folds and boudins. The error bars indicate one standard deviation (1σ). (For interpretation of the references to color in this figure legend, the reader is referred to the Web version of this article.)

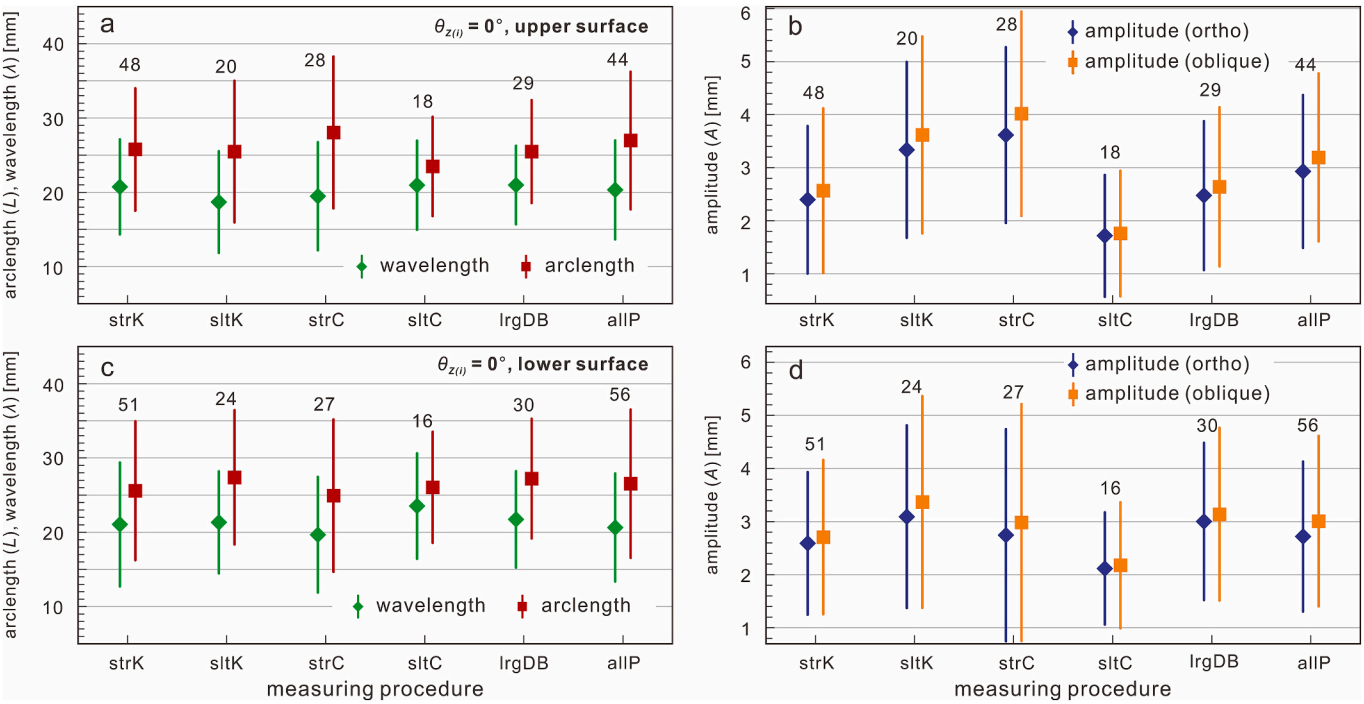

Fig. 6. Geometric data of non-cylindrical folds obtained from the upper surface (a–b) and the lower surface (c–d) shown in Fig. 4. Number of measurements, N, used to calculate mean values and standard deviation of the geometric data are indicated at the top of the plots. (a, c) Arc-length and wavelength; (b, d) Orthogonal and oblique amplitude. The different data shown in each diagram result from: preferred selection of strongly kinked (strK) and slightly kinked (sltK) measuring profiles; preferred selection of strongly curved (strC) and slightly curved (sltC) domes and basins; preferred profiles defined by distinct and relatively large domes and basins (lrgDB) and considered almost all possible profiles (allP). The error bars indicate one standard deviation (1σ).

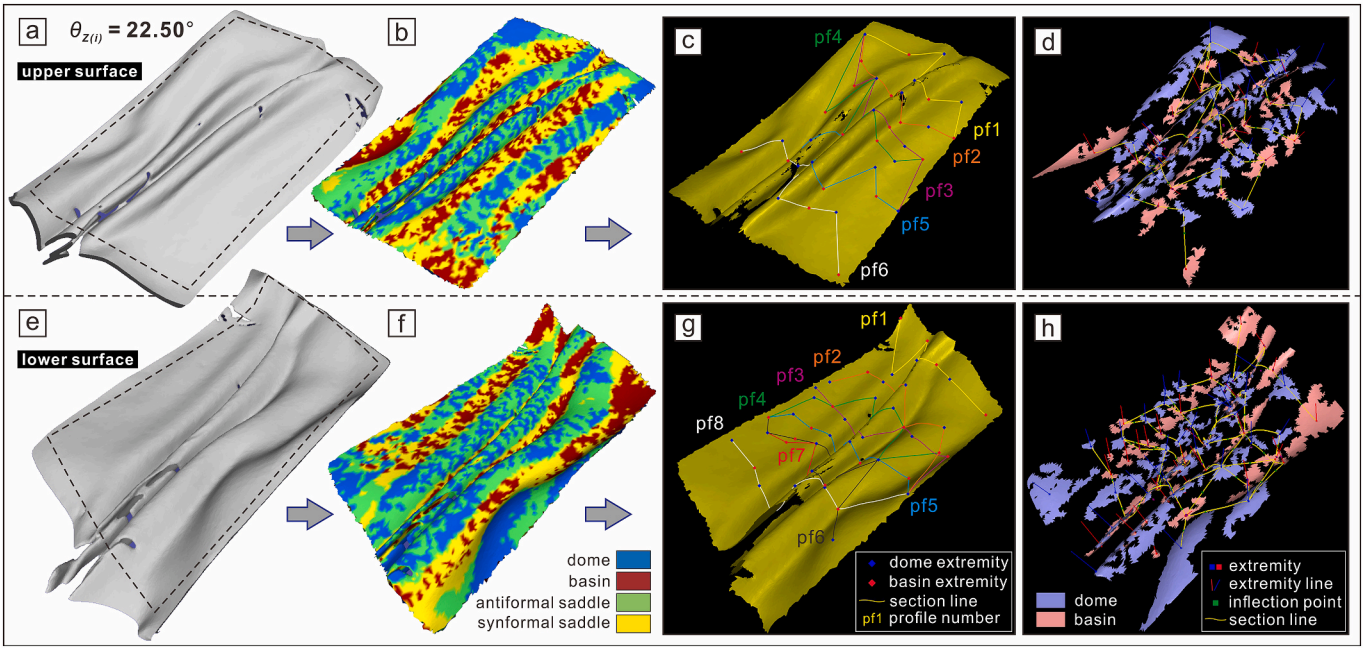

Fig. 7. 3D model of the deformed competent layer developing with typical folds without destruction by the boudins when $\theta_{Z(i)} = 22.50°$. The model is separated into the upper surface (a–d) and the lower surface (e–h) for a contrastive analysis. (a, e) The surface of the model which is constituted by numerous small polygons (triangles). Different grey levels result from different degrees of shading (inclination of the surface with respect to the light source). The dark blue dashed frame indicates the extent of detail for further 3D analyses. (b, f) Different fold types of the model depicting domes, basins, antiformal, and synformal saddles with different colors. (c, g) Gaussian curvature of the model exported from the software *Smoooth-AnalyzeModel* showing peaks of domes (blue) and basins (red). Peaks of domes, basins, and inflection points defining the lines with various colors indicate the different measuring profiles. (d, h) Separated domes (in blue) and basins (in pink) of the model. The extremities of domes and basins are shown by blue and red dots, respectively. The extremity lines of domes and basins are shown by blue and red lines, respectively. The yellow curved lines indicate selected measuring profiles. Inflection points are shown by green dots. (For interpretation of the references to color in this figure legend, the reader is referred to the Web version of this article.)

the F_{EPR} folds are affected by small-scale basins and synformal saddles depicted in red and yellow, respectively, in Fig. 7b–f. The synforms, on the other hand, show small-scale domes and antiformal saddles depicted in blue and green, respectively, in Fig. 7b–f.

Because of the insufficient number of F_{EPP} folds and in consideration of their statistically non-representative data, we primarily pay attention to the F_{EPR} folds when quantifying geometrical parameters of folds in the 3D model. Six profiles from the upper surface and eight profiles from the lower surface were selected according to the criterion that the profiles are perpendicular to the axes of the F_{EPR} folds (Fig. 7c,d,g,h). For the upper surface, the arc-length and wavelength values range from 21 to 33 mm and 17–29 mm, respectively, while the ortho and oblique amplitude values range between 1.8 and 2.2 mm and between 2.0 and 2.6 mm, respectively (Table S2, Supplement, Fig. 8a and b). The data obtained from the lower surface show similar values (Table S2, Supplement, Fig. 8c and d). In summary, the arc-length and wavelength from both surfaces yield mean values of 26 ± 9 mm and 22 ± 9 mm (Table S2, Supplement, Fig. 5c) and the ortho amplitude yields a mean value of 2.1 ± 1.2 mm (Fig. 5e).

By contrast, the F_{EPP} folds in this case formed as large open asymmetric folds and show differences with slightly longer arc-length and wavelength (ca. 56 mm and 54 mm, respectively; Table S1, Supplement, Fig. 5d), slightly lower amplitude (ca. 2.6 mm, Table S1, Supplement, Fig. 5e), and a considerably large interlimb angle of ca. 138° (Fig. 5f).

A further increase of $\theta_{Z(i)}$ to 33.75° is related to an increase in ductile and brittle elongation of the layer, which rotated towards the *X*-axis with a final angle of ca. 67°. This value is less than the value of a rotated passive plane (ca. 79°, Fig. 3c,d, 5a, Fig. S1, Supplement). Layer thickening was moderate at ca. 28% (Fig. 5b). The structures produced consist of tight, F_{EPR} folds and boudins separated by necks, which are aligned perpendicular to the *X*-axis. Most of the F_{EPR} folds are nearly cylindrical with an average arc- and wavelength of 19 ± 4 and 13 ± 6 mm, respectively (Fig. 5c–Fig. S1b,c). In comparison with the previous run ($\theta_{Z(i)}$ = 22.50°), the amplitude of the F_{EPR} folds is slightly decreased to 2.6 ± 1.2 mm (Fig. 5e). The F_{EPP} folds are gentle to open folds (δ = ca. 151°) characterized by increasing arc- and wavelength of ca. 91 mm and 89 mm, respectively, and a moderate amplitude of ca. 3.4 mm (Table S1, Supplement, Fig. 3d, 5d–f, S1d). Boudinage was in its initial stage. Most of the necks are not pervasive (Fig. 3c,d, Fig. S1) and the necks develop sporadically associated with a small number of boudins (Fig. 3c and 5h). As a consequence of the heterogeneous distribution of boudins and necks in this sample, as well as considerable boundary effects and large data uncertainties, no statistical analysis of boudins and necks was conducted in this run.

When $\theta_{Z(i)}$ was set to at 45.00°, the final state of layer thickening exhibited a decrease in comparison to the preceding runs and reached a value of ca. 18% (Fig. 5b). Rotation of the layer towards the *X*-axis was even larger than before with a final angle of ca. 77°, approaching gradually the attitude of the rotated passive layer (83°, Fig. 5a). The deformation structures consist of F_{EPR} folds, boudins and F_{EPP} folds. Most of the F_{EPR} folds are largely tight and are cut by the necks aligned almost perpendicular to the fold axes (Fig. 9a). The F_{EPR} folds are particularly frequent and well developed in the middle section of the layer with axes subparallel to the *X*-axis (Fig. 9a–c). Compared to the structures of the previous runs, the F_{EPR} folds in the present case are smaller with a shorter arc- and wavelength (16 ± 4 and 12 ± 4 mm, respectively; Fig. 5c). The amplitude is 2.1 ± 1.1 mm (Fig. 5e) and the interlimb angle increased to ca. 76° (Fig. 5f). The F_{EPP} folds are more open with longer arc- and wavelengths (118 ± 46 and 116 ± 44 mm, respectively; Fig. 9d,e, 5d). The amplitude (3.6 ± 1.2 mm, Table S1, Supplement, Fig. 5e) is similar to the amplitude of the F_{EPP} folds of the previous run but significantly higher than the amplitude of the F_{EPR} folds. The interlimb angle is much higher than that of the F_{EPR} folds (Fig. 5f), which explains its low numbers (Fig. 5h).

The elongation of the layer in the *X*-direction increased significantly compared with the previous run ($\theta_{Z(i)}$ = 33.75°) and is accommodated by both viscous and brittle deformation (Fig. 3c,d, 9a). Boudinage is restricted to the central part of the layer. The number of boudins and

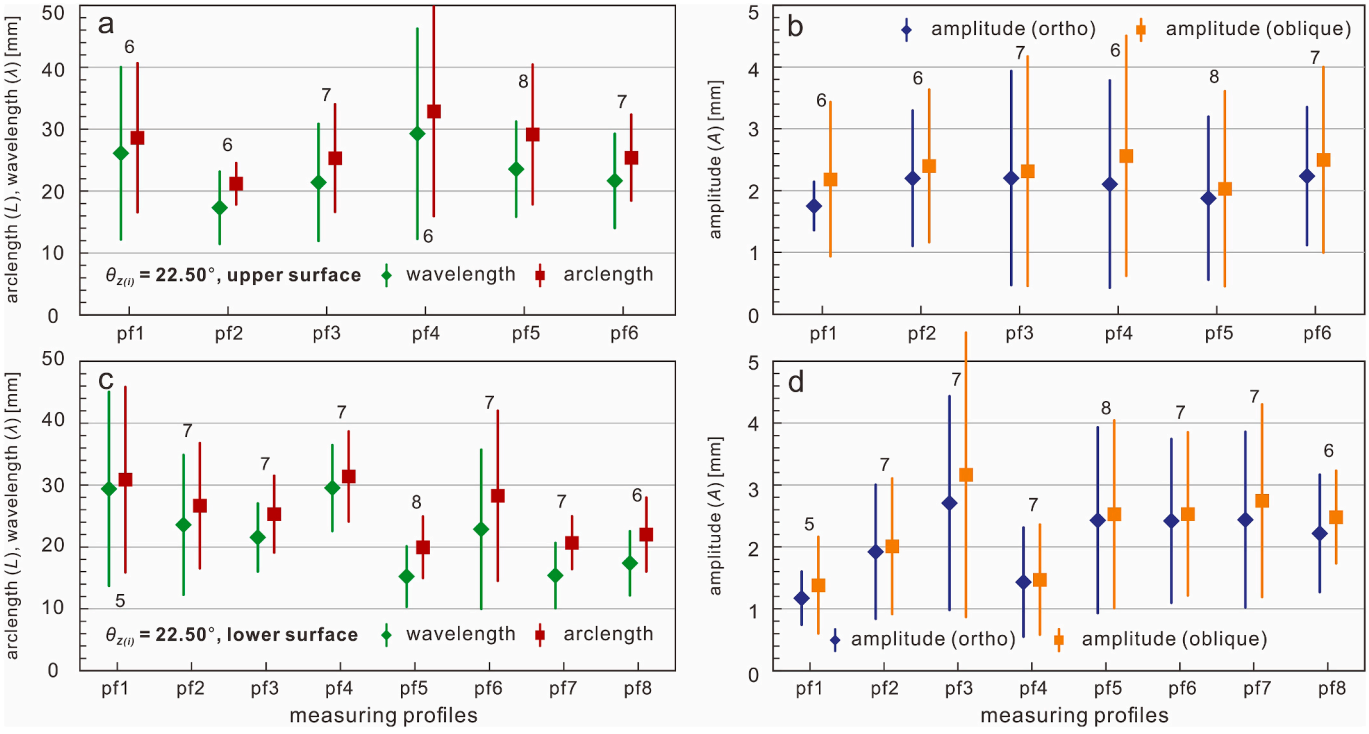

Fig. 8. Geometric data of non-cylindrical folds obtained from the upper surface (a–b) and the lower surface (c–d) shown in Fig. 7. Number of measurements, N, used to calculate mean values and standard deviation of the geometric data are indicated at the top or bottom of the plots. (a, c) Arc-length and wavelength; (b, d) Orthogonal and oblique amplitude. The different data shown in each diagram result from six profiles on the upper surface and eight profiles on the lower surface. The profiles parallel roughly to each other and all of them are orthogonal with the fold axes as far as possible. The error bars indicate one standard deviation (1σ).

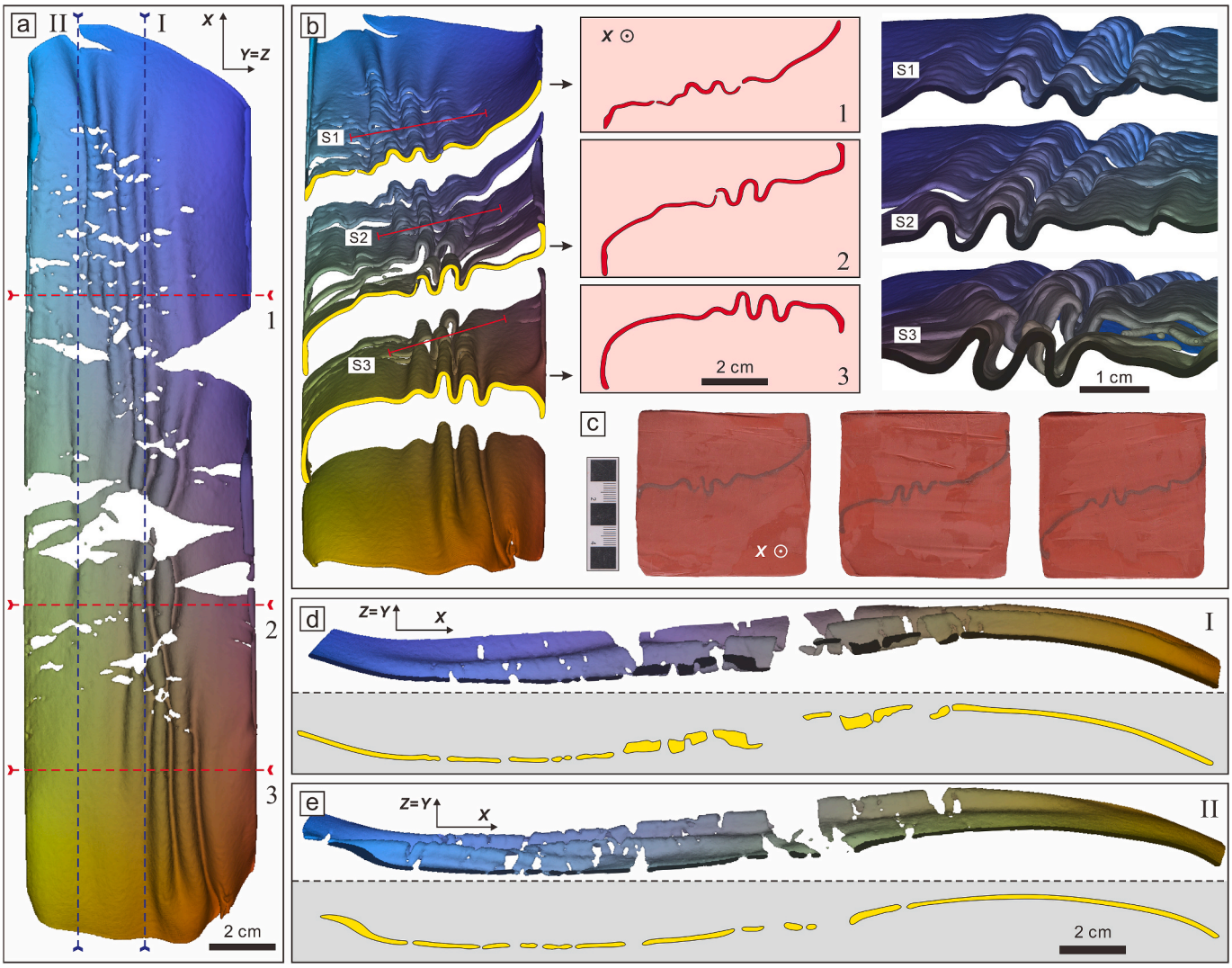

Fig. 9. Details of coeval folds and boudins of deformed competent layer when $\theta_{Z(i)} = 45.00°$. (a) CT image with the view subperpendicular to the layer showing extenison-parallel folds and boudins. Red dashed lines mark the position of the transections subperpendicular to the *X*-axis shown in (b). Dark blue dashed lines mark the position of the transections parallel to the *X*-axis and subparallel to the layer shown in (d) and (e). (b) CT images and schematic portray of the layer showing typical extension-prallel folds in sections subperpendicular to the *X*-axis. The positions of S1–S3 are marked as red solid lines in the leftmost column of (b). (c) Scanning photographs of sections showing details of extension-parallel folds of the competent layer. (d and e) Sections parallel to the *X*-axis and subparallel to the layer showing large-wavelength folds and boudins, both with axis subperpendicular to *X*. (For interpretation of the references to color in this figure legend, the reader is referred to the Web version of this article.)

necks significantly increased compared with the previous runs (Fig. 5h). The boudins and necks exhibit a markedly different width with relatively larger standard deviations (9 ± 8 mm and 3 ± 2 mm, respectively; Table S1, Supplement, Fig. 5g). Most boudins are barrel shaped and the necks are not always perpendicular to the *X*-axis but are more or less oblique. Some of the necks are not pervasive and die out within the layer (Fig. 9a).

When the layer was initially inclined at $\theta_{Z(i)} = 56.25°$, the degree of layer rotation was very close to that of a rotated passive layer (ca. 84° vs. 85° with respect to the *Z*-axis, Fig. 5a). The degree of layer thickening is ca. 24% (Fig. 5b). Deformation of the layer is still accommodated by buckling and boudinage (Fig. 3, Fig. S2, Supplement). The F_{EPR} folds are present as homoaxial $F1_{EPR}$ and $F2_{EPR}$ folds. The number of the short-wavelength $F1_{EPR}$ folds as well as their amplitudes do not display an obvious difference with the previous run, but they are more frequent and much smaller compared to the large-wavelength $F2_{EPR}$ folds (Figs. S2d and e). $F1_{EPR}$ folds are characterized by short arc- and wavelength (10 ± 3 and 8 ± 3 mm, respectively; Fig. 5c), and a low amplitude (1.2 ± 0.6 mm, Fig. 5e). The interlimb angle is ca. 92° (Fig. 5f). The $F2_{EPR}$ folds are present as large and open to gentle folds consistent with much longer arc- and wavelengths (49 ± 6 and 46 ± 7 mm, respectively; Fig. 5c), higher amplitude (3.0 ± 1.4 mm, Fig. 5e), and a larger interlimb angle (ca. 144°, Fig. 5f).

F_{EPP} folds are also present (Figs. S2b and c, Supplement). In comparison, the interlimb angle of the F_{EPP} folds is gradually increased over all previous runs (168 ± 4°, Fig. 5f) resulting in longer arc- and wavelengths (141 ± 39 and 140 ± 39 mm, respectively; Table S1, Supplement, Fig. 5c). Apart from the open F_{EPP} folds, described above, there is a 2nd type of F_{EPP} folds, referred to as FB_{EPP} folds, which affect the boudins (see red lines in Fig. 3c). The number of boudins increased compared to the previous runs (ca. 28, Table S1, Supplement, Fig. 5h). The boudins (ca. 8 mm) are still much wider than the necks (ca. 3 mm, Fig. 5g). Also in this case, there is a large number of necks, cracking from the edge of the layer, winding and dying out in the central part of the layer (Fig. 3c, Fig. S2a, Supplement). Consequently, most of the boudins are curved, forming a series of folds whose axes are subperpendicular to both the layer and the *X*-axis, respectively (Fig. S2a, Supplement).

When $\theta_{Z(i)}$ was set at 67.50°, rotation of the competent layer towards

the *X*-axis was almost identical to that of a passive plane (Fig. 5a), and the degree of thickening was the same as before (Fig. 5b). Bulk ductile shortening perpendicular to the *X*-axis and boudinage-related semi-brittle elongation along the *X*-axis are compatible with slight layer thickening. Small-wavelength $F1_{EPR}$ and large-wavelength $F2_{EPR}$ folds still coexist in this case (Fig. 3c and d). Although the interlimb angle of these folds increased (Fig. 5f), their number, arc-length, wavelength and their amplitude are similar to those described from the previous run (Fig. 5c–e,h). The same holds for the F_{EPP} folds (Table S1, Supplement, Fig. 5d–f).

The geometry of the boudins is also similar to that of the previous run with $\theta_{Z(i)} = 56.25°$ (Fig. 3c and d). However, the number of boudins and necks still increased (37 ± 3, Fig. 5h). The boudins yield a mean width of ca. 6 mm, while the necks average ca. 3 mm in width (Table S1, Supplement, Fig. 5g). Most of the boudins show well-rounded edges. Boudins in this case are also irregularly folded by the FB_{EPP} folds (see red lines in Fig. 3c).

Increasing $\theta_{Z(i)}$ sequentially to 78.75° still led to layer thickening (ca. 27%, Fig. 5b), but the layer barely rotated (Fig. 5a) and was elongated along the *X*-direction (Fig. 3). The geometrical parameters of $F1_{EPR}$ folds are similar to those of the previous run (Fig. 6c–e,f). The interlimb angle of the $F2_{EPR}$ folds increased (159 ± 8°, Fig. 5f) resulting in longer arc- and wavelengths (62 ± 8 and 60 ± 8 mm, respectively; Fig. 5c).

The arc- and wavelength (210 ± 91 and 209 ± 89 mm, respectively; Fig. 5d), amplitude (4.4 ± 1.9 mm, Fig. 5e), and interlimb angle (170 ± 3°, Table S1, Fig. 5f) of the large F_{EPP} folds show maximum values with a large standard deviation due to the heterogeneous occurrence and small number of folds. Because of the small amplitude and large arc- and wavelength, the average arc-length is almost equal to the average wavelength, and the interlimb angle is close to 180°.

As the layer was initially already subparallel to the *X*-axis and thus almost perpendicular to the shortening plane ($\theta_{Z(i)} = 78.75°$), boudinage was intensely developed (Fig. 3c and d). Consequently, the boudins and necks exhibit a similar width with the value of ca. 5.2 and 4.7 mm, respectively (Table S1, Supplement, Fig. 5g). The large standard deviation of the neck width, results from the inhomogeneous distribution of the boudins and the influence of the superimposed FB_{EPP} folds (Fig. 3c). As the boudins seem to have developed simultaneously with the F_{EPR} folds and are additionally affected by younger FB_{EPP} folds, with axes subperpendicular to the layer, necks appear also in the folded layer (Fig. 3c).

In the case that the layer was initially aligned parallel to the *X*-axis ($\theta_{Z(i)} = 90.0°$), there was no rotation during the deformation (Fig. 5a), but slight thickening occurred (ca. 8%, Fig. 5b). The number and geometry of the $F1_{EPR}$ and $F2_{EPR}$ folds are almost similar to those of the previous run. The amplitude of $F1_{EPR}$ folds decreased to a minimum value with the smallest standard deviation (2.7 ± 0.7 mm, Fig. 5e), leading to a smaller difference between arc- and wavelength (ca. 12.2 ± 2.6 and 11.9 ± 2.7 mm, respectively; Fig. 5c) and a larger interlimb angle (145 ± 12°, Fig. 5f). The latter is close to the interlimb angle of the $F2_{EPR}$ folds (ca. 157 ± 5°, Table S1, Supplement, Fig. 5f). As the layer is consistently aligned perpendicular to the plane of shortening (*YZ*-plane), F_{EPP} folds are lacking. However, the FB_{EPP} folds, which affect the boudins, are well developed with their axes perpendicular to the layer and to the *X*-axis (Fig. 3c).

The number of boudins reaches a maximum in this run (ca. 62, Table S1, Supplement, Fig. 5h). The boudins are shaped with tenuous and curved fragments, which are overprinted by FB_{EPP} folding as well (Fig. 3c and d). The boudins and necks exhibit almost the same width (4.3 and 3.7 mm, respectively), which is consistent with the previous experimental run (Fig. 5g).

3.2. Dimensionless and normalized geometrical parameters

The geometry of folds can be described by the dimensionless amplitude ($\underset{\sim}{A}$) (Schmalholz, 2006b), which is calculated by dividing the amplitude by the wavelength of the folds. The $\underset{\sim}{A}$ value of $F1_{EPR}$ folds increases slightly with $\theta_{Z(i)}$ until $\theta_{Z(i)} = 11.25°$ and then strongly decreases at $\theta_{Z(i)} = 22.50°$. After a strong increase at $\theta_{Z(i)} = 33.75°$, the $\underset{\sim}{A}$ values decrease consistently with increasing $\theta_{Z(i)}$ until the latter is 90.00° (Fig. 10a). The $\underset{\sim}{A}$ value of $F2_{EPR}$ folds, on the other hand, display lower values and do hardly change with increasing $\theta_{Z(i)}$. The F_{EPP} folds show high $\underset{\sim}{A}$ values if the layer is close to $\theta_{Z(i)} = 0°$. Increasing $\theta_{Z(i)}$ further to 22.50°, results in a significant drop in $\underset{\sim}{A}$, which remains similar low at higher $\theta_{Z(i)}$ (Fig. 10a).

The dominant wavelength of folds, corresponding to the maximal growth rate of folds, and the width of boudins can be related to the layer thickness and to the rheological parameters of the layer and matrix (Biot, 1961). The dominant wavelength is equivalent to the arc-length, which remains nearly constant during the kinematic growth of the fold, while the amplitude increases due to fold amplification

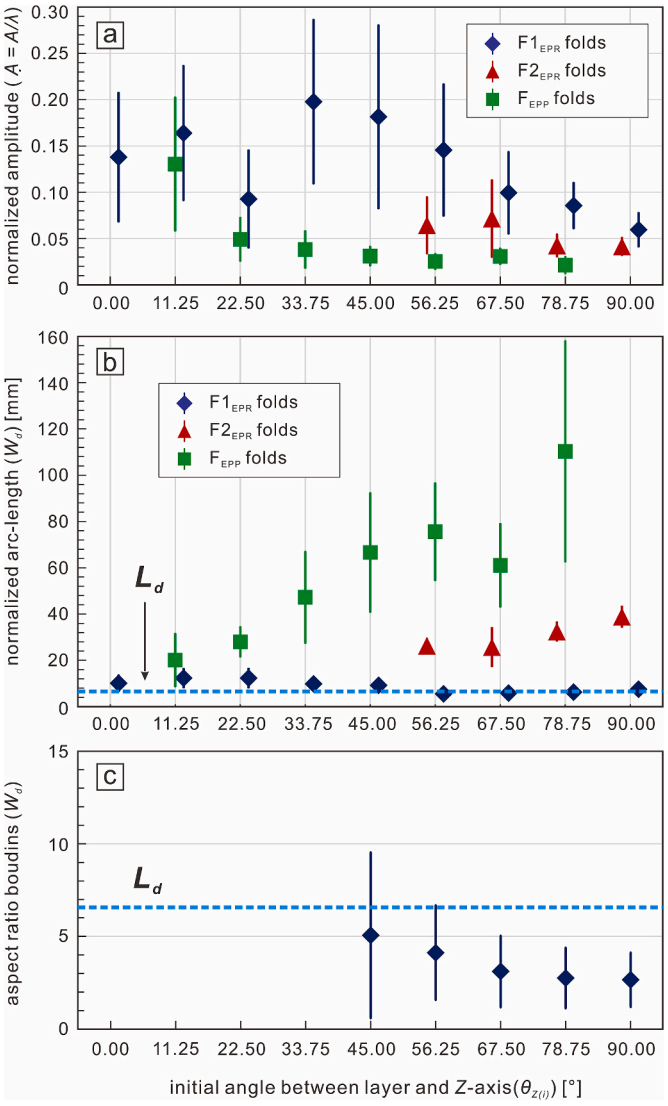

Fig. 10. (a) Normalized amplitude ($\underset{\sim}{A} = A/\lambda$) vs. initial orientation of layer ($\theta_{Z(i)}$) for the F_{EPR} and F_{EPP} folds. The shape of the depicted folds varies depending on $\underset{\sim}{A}$ (after Schmalholz, 2006b). (b) Relation between the initial orientation of layer ($\theta_{Z(i)}$) and normalized arc-length of the folds. The theoretical normalized arc-length (L_d) calculated using Eq. (1) is shown by the dashed blue line. (c) Relation between the initial orientation of layer ($\theta_{Z(i)}$) and normalized arc-length (= aspect ratio) of boudins. The theoretical normalized arc-length (L_d) calculated using Eq. (1) is shown by the dashed blue line. (For interpretation of the references to color in this figure legend, the reader is referred to the Web version of this article.)

(Schmalholz, 2006b). The dominant wavelength of both folds and boudins in non-linear materials is the same and can be calculated by the following equation (Smith, 1977):

$$L_d \approx 3.46\left(n_M^{1/6} \Big/ n_L^{1/3}\right)(\eta_L/\eta_M)^{1/3} \quad (1)$$

where L_d is the theoretical dimensionless wave length/finite thickness ratio, and n_L, η_L, and n_M, η_M are the stress exponents and the apparent viscosities in the flow laws for layer and matrix, respectively. According to the rheological parameters of the plasticine used in this study (Table S1, Supplement), L_d is calculated at 6.6.

To compare the geometrical parameters of folds and boudins developed in layers with different thickness, we use dimensionless values, the arc-length of folds and the width of boudins are divided by the finite layer thickness (H_f). The normalized arc-length (W_d) of $F1_{EPR}$ folds (L_{F1EPR}/H_f), $F2_{EPR}$ folds (L_{F2EPR}/H_f), F_{EPP} folds (L_{FEPP}/H_f), and the aspect ratio (W_d) of boudins (W_{Boudin}/H_f) are listed in Table S1 (Supplement) and are depicted in Fig. 10b and c.

The W_d values of $F1_{EPR}$ folds are similar or slightly higher than the L_d value (Fig. 10b). With increasing initial orientation of the layer ($\theta_{Z(i)}$ = 56.25°, 67.50°, and 78.75°) the W_d value of the $F1_{EPR}$ folds display lower values and the discrepancy between L_d and W_d is lower (Fig. 10b). In cases where $\theta_{Z(i)}$ was >45.00°, the W_d values match or are close to the L_d value (Fig. 10b–Table S1, Supplement). The W_d values of $F2_{EPR}$ folds are considerably higher with a large discrepancy between L_d and W_d. They show increasing values along with increasing initial obliquity of the layer (Fig. 10b). When the layer is initially parallel to the X-axis ($\theta_{Z(i)}$ = 90°), the W_d value reaches a maximum and presents the largest discrepancy between W_d and L_d (Fig. 10b). The W_d values of the F_{EPP} folds display an increasing tendency along with increasing obliquity of the layer, and the W_d values are significantly higher than the L_d value for all runs (Fig. 10b). The minimum W_d value (ca. 20) occurs if $\theta_{Z(i)}$ was set at 11.25° and the maximum with ca. 110 is attained if $\theta_{Z(i)}$ is 78.75° (Table S1, Supplement, Fig. 10b). The aspect ratios of boudins show decreasing values with increasing initial layer obliquity (Fig. 10c). All of the W_d values range between 2 and 6 and thus are generally below the L_d value (Table S1, Supplement, Fig. 10c).

4. Discussion

4.1. Syn-deformational layer thickening

In all experiments of the present study, the initial thickness of the competent layer increased during the deformation. The highest degree of layer thickening (ca. 76%) occurred when $\theta_{Z(i)}$ = 0°, whereas the lowest degree of thickening (ca. 8%) occurred at $\theta_{Z(i)}$ = 90.00° (Fig. 5b). Moreover, the new results suggest that only a slight initial inclination of the layer with respect to principal strain axes ($\theta_{Z(i)}$ = 11.25° or 78.75°) results in a significant change in layer thickness (Fig. 5b). In the first case ($\theta_{Z(i)}$ = 11.25°), there is a reduction in thickening by about 50% compared to the non-oblique layer ($\theta_{Z(i)}$ = 0°). At higher values of $\theta_{Z(i)}$, the degree of layer thickening gradually decreased until $\theta_{Z(i)}$ approaches 45° (Fig. 5b). Subsequently, the degree of layer thickening slightly increased and sustained with almost similar values until $\theta_{Z(i)}$ was 78.75° (Fig. 5b). The second case of significant reduction in layer thickening by about 20% occurs when $\theta_{Z(i)}$ = 90° (Fig. 5b; Table S1, Supplement).

There are several parameters, including viscosity ratio, layer-parallel shortening along the Y=Z-axis without buckling, and layer-parallel elongation along the X-axis without boudinage, that control the changes in layer thickness during progressive deformation (Zulauf et al., 2021). As the apparent viscosity ratio is constant at 18 throughout the experiments, we will not consider its effect on layer thickening. Since the experiments are conducted under bulk coaxial constriction with finite strain $e_Z = e_Y = -50\%$, the amount of shortening along the Y=Z-axis is the same in each run (Fig. 1a). Thus, it is essential to take into account the amount of ductile layer-parallel elongation along the X-axis. The layer-parallel elongation changed from run to run due to the gradual change in initial layer inclination and related variation in layer rotation towards the X-axis.

In cases of $\theta_{Z(i)} \leq 45.00°$, thickening of the competent layer should have occurred before the onset of the $F1_{EPR}$ folding (e.g. Ramsay, 1974; Hudleston, 1986; Ramsay and Huber, 1987; Schmalholz, 2006a). Because of significant layer rotation, the geometry of the $F1_{EPR}$ folds changed during progressive constriction. The degree of layer thickening shows a declining trend with increasing values of $\theta_{Z(i)}$ (Fig. 3c,d, 5b). If 45.00° < $\theta_{Z(i)}$ < 90.00°, the $F2_{EPR}$ folds overprint the preexisting $F1_{EPR}$ folds including the thickened layer. In these cases, both the F_{EPR} and F_{EPP} folds exhibit gentle to open geometry with a large interlimb angle (Fig. 5f), reflecting the thickening of the layer. On the other hand, when the $\theta_{Z(i)}$ > 33.75°, the layer-parallel elongation is distinctly evident and triggers the onset of boudinage (Fig. 3c and d). In the case of $\theta_{Z(i)}$ = 90.00°, the layer-parallel shortening along the Y=Z-axis attains the minimum value, whereas the layer undergoes maximum elongation along the X-axis. As the layer-parallel elongation along the X-axis is not only accommodated by ductile stretch but also by boudinage, layer-parallel shortening along the Y=Z-axis results in both layer thickening and F_{EPR} folds (Fig. 5b).

4.2. Coeval growth of folds and boudins in bulk constriction

Two different types of folds were produced if the layer is inclined in a constrictional strain field. The first type of folds with axes subparallel to the X-axis (F_{EPR} folds) are present as short-wavelength $F1_{EPR}$ folds, which are overprinted by the larger homoaxial $F2_{EPR}$ folds when the $\theta_{Z(i)}$ > 45° (Fig. S2e). The parasitic $F1_{EPR}$ and refolding $F2_{EPR}$ folds are related to Type 0 fold interference patterns (Thiessen and Means, 1980), which are common in naturally deformed rocks (e.g. Schmalholz and Mancktelow, 2016). The second type of folds has axes subperpendicular to the X-axis (F_{EPP} folds), which developed when $\theta_{Z(i)}$ < 90°. Apart from the open F_{EPP} folds, there is a 2nd type of F_{EPP} folds developed when the $\theta_{Z(i)}$ > 45°, which are affecting the boudins (FB_{EPP} folds, Fig. 3c).

Taking into account the boundary effects during deformation, we selected the middle portion of the layer in all samples for statistical analysis of boudins and folds (e.g. Fig. 9a–Fig. S1a, S2a, Supplement). The interlimb angles of all types of folds increase with increasing initial obliquity of the layer. In cases where the inclination of the layer $\theta_{Z(i)}$ is > 22.50°, F_{EPR} folds and boudins grow simultaneously. The boudin axes are aligned perpendicular to the X-axis within the YZ-plane and the boudins are larger with increasing initial layer obliquity (Fig. 5g). Several boudins with barrel-shaped geometry possess straight faces and rounded edges, suggesting that the thinned neck domain has been brittlely fractured by a tensile fracture following viscous necking (Ramberg, 1955; Rast, 1956; Paterson and Weiss, 1968; Strömgård, 1973; Burg and Harris, 1982; Dieter, 1986; Zulauf et al., 2011, 2014). Boudinage accommodated by pure tensile fracture, on the other hand, should result in boudins with extremely small aspect ratios close to 1 (Bai et al., 2000).

Depending on its initial orientation, the competent layer rotates similar fast or slower than a corresponding passive plane during bulk constriction (Fig. 5a). A similar behavior has been documented by previous modelling and experimental investigations under bulk plane strain in which the layer rotates around the Y-axis (e.g. Cobbold et al., 1971; Watkinson, 1975, 1976; Frehner and Schmalhoz, 2006; Mandal et al., 2007; Zulauf et al., 2020a). On the other hand, if during progressive plane strain, the layer rotates around the Z- or X-axis, its rate of rotation is similar to that of a passive plane (Zulauf et al., 2020b, 2021). In this study, the geometry of folds and boudins is significantly controlled by the degree of layer rotation during progressive constriction, which depends on the magnitude of finite strain and the initial inclination of the layer. Under bulk constriction, simultaneous growth of folds and boudins is reasonable if the competent layer is aligned parallel to the X-axis (Fig. 1a and 3; Fletcher, 1995; Kobberger and Zulauf, 1995; Zulauf and

Zulauf, 2005). If, on the other hand, the competent layer is oriented perpendicular to the *X*-axis, pure constriction results in dome-and-basin structures (Fig. 1a and 3; Ghosh et al., 1995; Schmalholz, 2008; Schmid et al., 2008; Zulauf et al., 2016).

Folds and boudins of the present study were formed under bulk constriction and thus exhibit 3D structures. Folding and boudinage in 3D strain fields have been investigated theoretically by Flinn (1962). A further theoretical study, restricted to folding, was carried out by Treagus and Treagus (1981), who regarded the fold axis as active lines. When the *lines of no finite deformation* and the *lines of no infinitesimal deformation* for a bulk constrictional deformation ellipsoid are plotted on an equal-area net, they divide the net into three different areas referred to as *the area of elongation*, *the area of reduced shortening*, and *the area of shortening* (Flinn, 1962). These domains are shown in orange red, violet, and light blue in Fig. 11.

During progressive bulk constriction, the axes of single boudins are distributed along the circumference of the net, while single fold axes are restricted to the elongation area, and double fold axes are plotting in the shortening and reduced shortening areas (Fig. 11). The layers with their initial orientation as used in the present study are shown with different colors in Fig. 11a. The orientation of these layers after deformation is shown in Fig. 11b (passive plane) and in Fig. 11c (non-passive plane).

To delineate the progressive rotation and deformation state of a passive plane, a schematic diagram has been drawn, in which an ellipsoid (ellipse) and passive planes (lines) with different initial obliquity were incrementally deformed by multiples of $e_{Y=Z} = -10\%$ until the final constrictional strain ($e_{Y=Z} = -50\%$) was attained (Fig. 12). The angles between the rotated passive planes and the *Y*=*Z*-axis ($\theta_{Z(RPL)}$) are measured from the final deformed state of the passive layer and listed in Table S1 (Supplement) and are added to the diagram shown in Fig. 5a.

In addition, the longitudinal strain (e_L) and rotation of the passive layer ($\theta_{Z(RPL)}$) are plotted vs. the bulk constrictional strain ($e_{Y=Z}$) in Fig. 13a and b, respectively. The diagram in Fig. 13a shows that, apart from the non-oblique plane ($\theta_{Z(i)} = 0°$), which was shortened, and the slightly oblique plane ($\theta_{Z(i)} = 11.25°$), which was involved in reduced shortening, all other passive planes sustained elongation until the final strain of $e_{Y=Z} = -50\%$ was attained. Except for the case when $\theta_{Z(i)} = 0°$, the rate of layer rotation significantly increases with finite strain when the initial obliquity $\theta_{Z(i)}$ is less than 45° (Fig. 13b). If $45° < \theta_{Z(i)} < 90°$, the rotation rate of the layer is restricted (Fig. 13b).

In the case of $\theta_{Z(i)} = 0.00°$, the layer did not rotate and remained completely in the area of shortening, which is projected as a large concentric circle (Fig. 11b). The layer that was initially oriented at $\theta_{Z(i)} = 11.25°$, remained in the fields of shortening and reduced shortening (Fig. 11b). In other words, parts of this layer are shortened throughout, and other parts are first shortened and then elongated, but elongation is insufficient to attain the original length (Zulauf et al., 2020b). All other layers, however, are affected by various kinematics and cross all the three strain fields during rotation and thus prominently indicate the deformation is inhomogeneous and complex (Fig. 11b). Lines with different orientations within the layer show different kinematics. Layers which are oriented close to *X*-axis are affected by shortening, reduced shortening and elongation. This is the reason, why folds and boudins grow simultaneously. Folds consist of $F1_{EPR}$ and $F2_{EPR}$ folds with axes subparallel to the *X*-axis, and boudins display axes subperpendicular to the *X*-axis. As soon as boudins have been developed, the shortening strain along the boudin axes results in buckling of the boudins with fold axes pependiuclar to the *X*-axis and to the layer (FB_{EPP} folds). Thus FB_{EPP} folds are late structures of the constrictional deformation. These results are consistent with those obtained from previous constrictional experiments (Kobberger and Zulauf, 1995; Zulauf and Zulauf, 2005).

The large-wavelength F_{EPP} folds, which are characteristic for oblique layers, result from shortening in a direction oblique to the layer rather than layer-parallel shortening. This type of folding is particularly strong during the initial phase of deformation when the layer has not rotate much. As the layer is oblique to the shortening direction, most of the folds are asymmetric. With increasing $\theta_{Z(i)}$, the layer is oriented more and more parallel to the *X*-axis and the component of oblique shortening

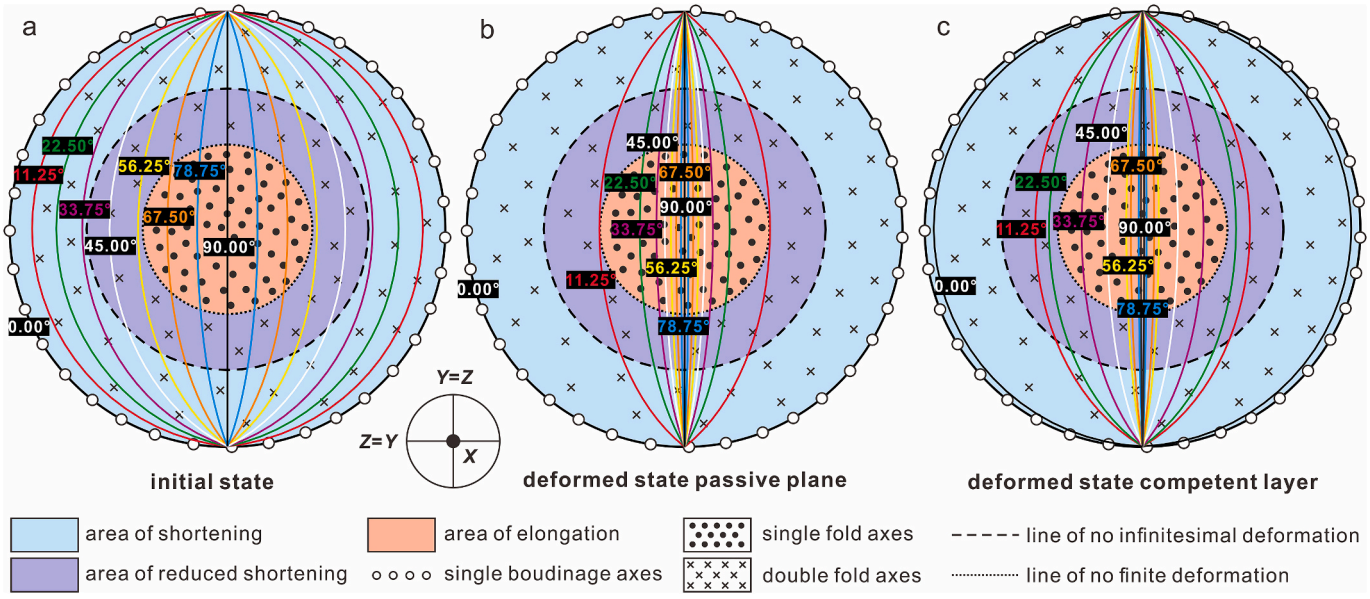

Fig. 11. Folds and boudins in bulk constrictional strain field. The distribution of possible fold and boudinage axes is shown in relation to the lines of no finite and no infinitesimal deformation in equal-area net (after Flinn, 1962). $X > Y = Z$ are the axes of principal strain; the *X*-axis is vertical in the equal-area net. Light blue color indicates lines in the field of shortening. Dark purple color indicates lines in the field of reduced shortening. Orange color indicates lines in the field of elongation. (a) Undeformed state showing the initial orientation of competent layers used for the different experimental runs. Great circles of competent layers are shown in different colors. Numbers in black boxes indicate the initial angle between the layer and the $Y = Z$-plane ($\theta_{Z(i)}$). (b) Deformed state showing the position of *passive planes* that were initially oriented like the competent layers used in the present study. The color of the great circles corresponds to that used for the great circles shown in (a). Numbers in black boxes indicate the angle between the passive plane and the $Y = Z$-plane. (c) Deformed state showing the position of the *competent layers*. The color of the great circles corresponds to that used for the great circles shown in (a). Numbers in black boxes indicate the finite angle between the layer and the *Z*-axis. (For interpretation of the references to color in this figure legend, the reader is referred to the Web version of this article.)

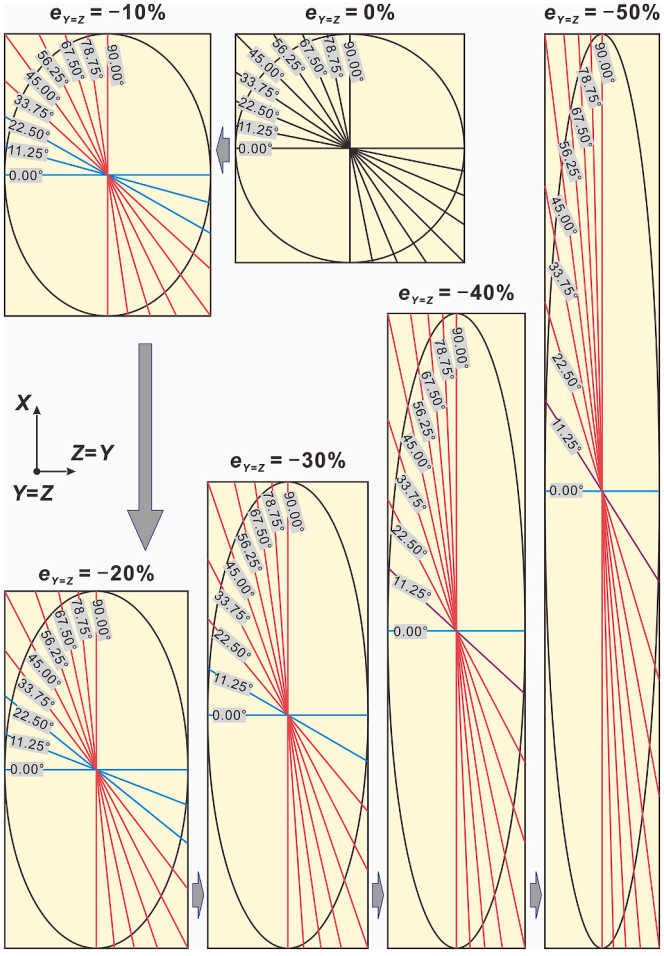

Fig. 12. Incremental deformation of a passive plane (or line) under bulk constrictional strain at increments of $e_Z = -10\%$ shown in sections parallel to the *X*-axis. The latter is vertical in each figure. The initial angle between the planes (lines) and the *Z*-axis ($\theta_{Z(i)}$) is indicated. Note that the amount of shortening along the *Y*-axis is the same like the amount of shortening along the *Z*-axis, which is oriented perpendicular to the plane of projection.

decreases. The F_{EPP} folds are open and gentle gradually with larger wavelength, arc-length and interlimb angle, but lower amplitude with increasing $\theta_{Z(i)}$ (Fig. 5d–f). It should be noted, however, that parts of these folds are probably not related to buckling, but result from the boundary effect along the face of the sample that is not confined by the walls of the machine. The elongation of the layer along the *X*-axis decreases from the central part of the sample towards the margin (which is perpendicular to the *X*-axis) and ceases at the margin. This reduction in *X*-parallel elongation is well documented by decreasing amounts of boudins at both ends of the sample. Because of this reduction in elongation, the rotation of the layer should be also affected and could have contributed to its bending in sections cut parallel to the *X*-axis and perpendicular to the layer.

4.3. Natural examples of coeval folding and boudinage of oblique single layers in bulk constrictional strain fields

Rocks deformed under non-plane conditions are frequent in nature. Constricitional strain is common in subduction tectonites (Zulauf, 1997; Zulauf et al., 2002, and references therein), in foliation triple points of more than two interfering gneiss domes (Bouhallier et al., 1995), and in the internal parts of salt domes (Balk, 1949; Talbot and Jackson, 1987). In the case of salt domes, an oblique competent layer of halite-dominated rock salt could be folded and boudinaged in a matrix of sylvite and carnallite, or a competent layer of anhydrite could be folded and boudinaged as a 'stringer' in a matrix of rock salt (Fig. 14a). The competent felsic vein embedded in the gneiss and schist could be deformed into lens shaped boudins and pinch-and-swell structures, which are affected by open to gentle folding with the fold axes subparallel to the boudin axes (Fig. 14b). Moreover, non-cylindrical folds could be formed in quartz mica schist layers which display approximate oblique dome-and-basin structures (Fig. 14c).

According to the outcome of the present study, the dome-and-basin structures can be formed if the competent layer is oriented parallel or nearly parallel to the *YZ*-plane in a bulk constrictional strain field. It should be noted, however, that apart from single-phase formation under bulk constriction, dome-and-basin structures may result from polyphase folding and related interference pattern (e.g. Lim and Cho, 2012; Bose et al., 2014; Shaanan et al., 2014). In contrast to constrictional dome-and-basin structures, constrictional coeval folds and boudins are more common in nature. Well documented samples include the ptygmatic folds from the southern Prince Charles Mountains (Corvino et al., 2016), the folded boudinage of migmatites in the high strain Taili deformation zone in Northern China (Li et al., 2023), and the folded boudin in siltstone/sandstone from the Neoproterozoic rocks of the Jabal Akhdar Dome, Oman Mountains (Scharf et al., 2021).

5. Conclusions

The results of the present study suggest that bulk constriction of a competent layer embedded in a weaker matrix results in complex non-cylindrical folds and boudins if the layer is oblique to the principal strain axes. The following conclusions can be drawn.

- In bulk constrictional strain fields, the initial angle between a competent layer and the shortening axis ($\theta_{Z(i)}$) is an important parameter for finite layer thickness and the type and geometry of folds and boudins.
- Compared with a passive plane, the retarded rotation of the competent layer during progressive deformation has a significant impact on the deformation structures. The degree of layer rotation is controlled by the finite strain (e_Z) and the initial orientation of the layer ($\theta_{Z(i)}$).
- The layer underwent thickening in all of the experimental runs. The highest and lowest degree of thickening occurred when the $\theta_{Z(i)} = 0°$ and 90°, respectively. Only small inclinations either away from the *X*-axis or away from the *YZ*-plane result in a strong change in the degree of layer thickening.
- There are generally two different types of folds if the layer is inclined in a constrictional strain field. Folds with axes parallel to the *X*-axis are present as low-wavelength $F1_{EPR}$ folds, which are overprinted by the larger homoaxial $F2_{EPR}$ folds when the $\theta_{Z(i)} > 45°$. The second type of folds (F_{EPP} folds) display axes perpendicular to the *X*-axis and occur if $\theta_{Z(i)} < 90°$. The interlimb angles of all types of folds increase with increasing initial obliquity of the layer.
- If $\theta_{Z(i)}$ is > 22.50°, F_{EPR} folds and boudins grow simultaneously. The boudin axes are aligned perpendicular to the *X*-axis within the *YZ*-plane.
- Boudinage results from initial viscous necking succeeded by fracturing. The width of the boudins decreases with increasing initial layer obliquity. Most of the boudins are affected by FB_{EPP} folds, with axes perpendicular to the layer.
- The data and results of the present study can be used to identify the setting and development of folds and boudins found in nature. As quantitative geometrical data obtained from 3D models of natural examples can be compared with those of the present study, the latter help to improve our understanding of boudinage and non-cylindrical folding in three-dimensional strain fields.

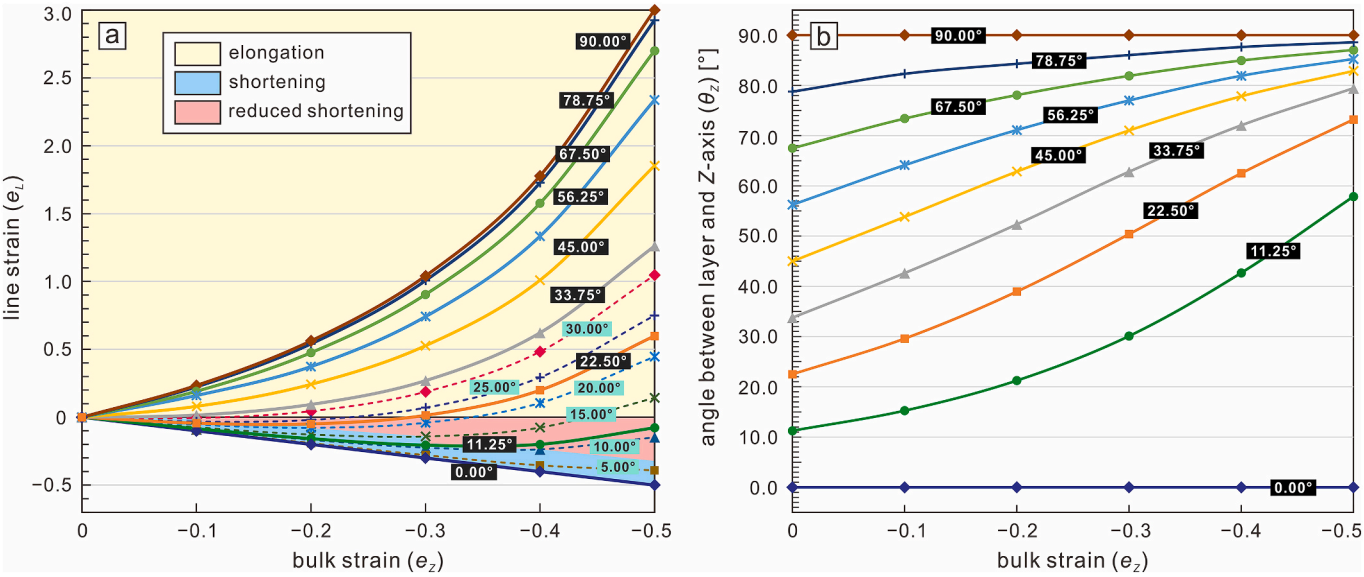

Fig. 13. (a) Bulk constrictional strain, $e_{Y=Z}$, vs. strain of passive line (or plane) in *XZ*-section. The angle between the plane and the *Z*-axis ($\theta_{Z(i)}$) is indicated by the numbers in black boxes on the lines. Apart from planes, which initially differ at 11.25° increments, we have added planes, which initially differ at 5°. The strain paths of the latter are depicted with dashed lines and the angle is indicated in blue-green boxes on the lines. Blue color indicates planes in the field of shortening. Pink color indicates planes in the field of reduced shortening. Yellow color indicates planes in the field of elongation. (b) Bulk constrictional strain, $e_{Y=Z}$, vs. angle between passive line (or plane) and *Z*-axis ($\theta_{Z(RPL)}$). The angle between the plane and the *Z*-axis ($\theta_{Z(i)}$) is indicated by the numbers in black boxes on the lines. (For interpretation of the references to color in this figure legend, the reader is referred to the Web version of this article.)

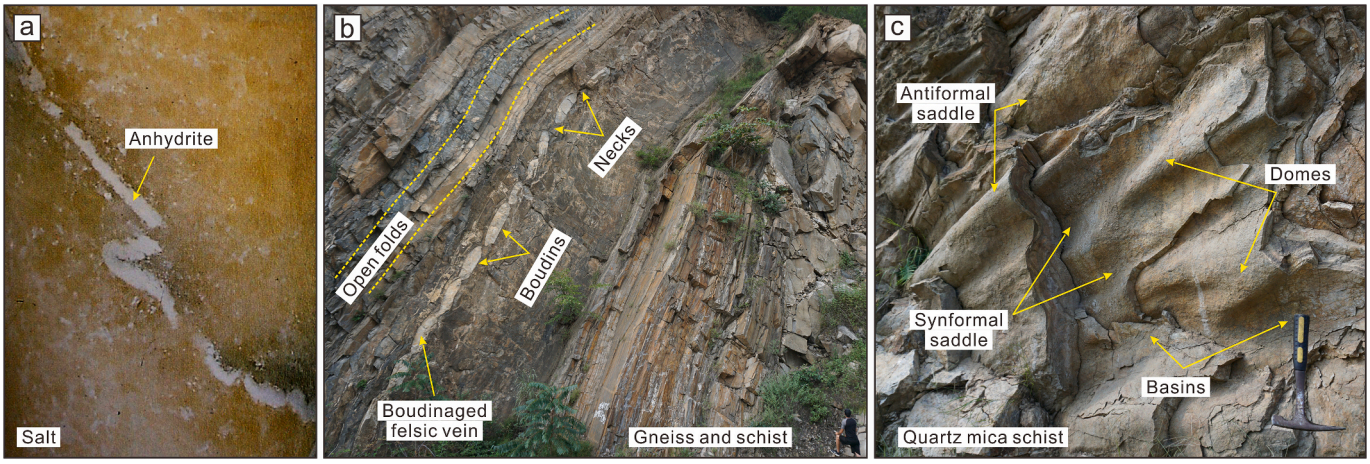

Fig. 14. Natural examples of competent single layers embedded in incompetent matrix deformed under bulk constrictional strain. (a) Thin single anhydrite layer from a drill core in Orange Salt of the Gorleben salt stock, Germany; width of the drill core = 10 cm. (b) Boudinaged felsic vein in gneiss and schist shows open fold with axes subparallel to the boudin axes. (c) Non-cylindrical folds in quartz mica schist layers display approximate oblique dome-and-basin structures. Photos (b) and (c) were taken from the Qinling Complex, central China. (For interpretation of the references to color in this figure legend, the reader is referred to the Web version of this article.)

CRediT authorship contribution statement

Chao Cheng: Writing – review & editing, Writing – original draft, Visualization, Validation, Resources, Methodology, Investigation, Formal analysis, Data curation. **Janet Zulauf:** Writing – review & editing, Validation, Supervision, Resources, Methodology, Formal analysis. **Gernold Zulauf:** Writing – review & editing, Validation, Supervision, Resources, Project administration, Funding acquisition, Conceptualization. **Elke Hattingen:** Validation, Supervision, Software, Methodology.

Declaration of competing interest

The authors declare that they have no known competing financial interests or personal relationships that could have appeared to influence the work reported in this paper.

Data availability

Data will be made available on request.

Acknowledgements

We acknowledge JSG editor Toru Takeshita, reviewers Fernando O. Marques and Marcin Dabrowski for their constructive comments and valuable feedback that we have used to improve the quality of our manuscript. We thank the help of Mark Peinl when using his software *Smoooth*. The studies were supported by a grant from Deutsche

Forschungsgemeinschaft, Germany (DFG, grant Zu 73/38).

Appendix A. Supplementary data

Supplementary data to this article can be found online at https://doi.org/10.1016/j.jsg.2024.105153.

References

Abe, S., Urai, J.L., 2012. Discrete element modeling of boudinage: Insights on rock rheology, matrix flow, and evolution of geometry. J. Geophys. Res. Solid Earth 117, 1–13. https://doi.org/10.1029/2011JB008555.

Adamuszek, M., Schmid, D.W., Dabrowski, M., 2011. Fold geometry toolbox - automated determination of fold shape, shortening, and material properties. J. Struct. Geol. 33, 1406–1416. https://doi.org/10.1016/j.jsg.2011.06.003.

Alsop, G.I., Strachan, R.A., Holdsworth, R.E., Burns, I.M., 2021. Geometry of folded and boudinaged pegmatite veins emplaced within a strike-slip shear zone: a case study from the Caledonian orogen, northern Scotland. J. Struct. Geol. 142, 104233 https://doi.org/10.1016/j.jsg.2020.104233.

Anthony, M., Wickham, J., 1978. Finite-element simulation of asymmetric folding. Tectonophysics 47, 1–14. https://doi.org/10.1016/0040-1951(78)90148-8.

Arango, C., Díez Fernández, R., Arenas, R., 2013. Large-scale flat-lying isoclinal folding in extending lithosphere: Santa María de la Alameda dome (Central Iberian Massif, Spain). Lithosphere 5 (5), 483–500. https://doi.org/10.1130/L270.1.

Bai, T., Pollard, D.D., Gao, H., 2000. Explanation for fracture spacing in layered materials. Nature 403, 753–756. https://doi.org/10.1038/35001550.

Balk, R., 1949. Structure of grand saline salt dome, van zandt county, Texas. Bull. Am. Assoc. Pet. Geol. 33, 1791–1829.

Biot, M.A., 1961. Theory of folding of stratified viscoelastic media and its implications in tectonics and orogenesis. Geol. Soc. Am. Bull. 72, 1595–1620.

Bose, S., Mandal, N., Acharyya, S.K., Ghosh, S., Saha, P., 2014. Orogen-transverse tectonic window in the Eastern Himalayan fold belt: a superposed buckling model. J. Struct. Geol. 66, 24–41. https://doi.org/10.1016/j.jsg.2014.05.008.

Bouhallier, H., Chardon, D., Choukroune, P., 1995. Strain patterns in archaean dome-and-basin structures: the Dharwar craton (Kamataka, South India). Earth Planet Sci. Lett. 135, 57–75.

Burg, J.P., Harris, L.B., 1982. Tension fractures and boudinage oblique to the maximum extension direction: an analogy with lüders' bands. Tectonophysics 83, 347–363. https://doi.org/10.1016/0040-1951(82)90027-0.

Carter, N.L., Tsenn, M.C., 1987. Flow properties of continental lithosphere. Tectonophysics 136, 27–63. https://doi.org/10.1016/0040-1951(87)90333-7.

Cobbold, P.R., Cosgrove, J.W., Summers, J.M., 1971. Development of internal structures in deformed anisotropic rocks. Tectonophysics 12, 23–53. https://doi.org/10.1016/0040-1951(71)90065-5.

Corvino, A.F., Boger, S.D., Fay, C., 2016. Constriction structures related to viscous collision, southern Prince Charles Mountains, Antarctica. J. Struct. Geol. 90, 128–143. https://doi.org/10.1016/j.jsg.2016.08.005.

Dieter, G.E., 1986. Mechanical Metallurgy. In: McGraw-Hill Series in Material Science and Engineering. McGraw-Hill, Boston, pp. 1–646.

Druguet, E., Alsop, G.I., Carreras, J., 2009. Coeval brittle and ductile structures associated with extreme deformation partitioning in a multilayer sequence. J. Struct. Geol. 31 (5), 498–511. https://doi.org/10.1016/j.jsg.2009.03.004.

Enama Mengong, M., Zulauf, G., 2006. Coeval folding and boudinage under plane strain with the axis of no change perpendicular to the layer. Int. J. Earth Sci. 95, 178–188. https://doi.org/10.1007/s00531-005-0032-z.

Fletcher, R.C., 1974. Wavelength selection in the folding of a single layer with power-law rheology. Am. J. Sci. 274, 1029–1043.

Fletcher, R.C., 1995. Three-dimensional folding and necking of a power-law layer: are folds cylindrical, and, if so, do we understand why? Tectonophysics 247, 65–83. https://doi.org/10.1016/0040-1951(95)00021-E.

Flinn, D., 1962. On folding during three-dimensional progressive deformation. Q. J. Geol. Soc. Lond. 118, 385–428. https://doi.org/10.1144/gsjgs.118.1.0385.

Frehner, M., Schmalholz, S.M., 2006. Numerical simulations of parasitic folding in multilayers. J. Struct. Geol. 28, 1647–1657. https://doi.org/10.1016/j.jsg.2006.05.008.

Ghosh, S.K., Khan, D., Sengupta, S., 1995. Interfering folds in constrictional deformation. J. Struct. Geol. 17, 1361–1373. https://doi.org/10.1016/0191-8141(95)00027-B.

Goscombe, B.D., Passchier, C.W., 2003. Asymmetric boudins as shear sense indicators—an assesment from field data. J. Struct. Geol. 25 (4), 575–589. https://doi.org/10.1016/S0191-8141(02)00045-7.

Grujic, D., Mancktelow, N.S., 1995. Folds with axes parallel to the extension direction: an experimental study. J. Struct. Geol. 17, 279–291. https://doi.org/10.1016/0191-8141(94)E0048-4.

Hubbert, M.K., 1937. Theory of scale models as applied to the study of geologic structures. Bull. Geol. Soc. Am. 48, 1459–1520. https://doi.org/10.1130/GSAB-48-1459.

Hudleston, P.J., 1973. An analysis of "Single-layer" folds developed experimentally in viscous media. Tectonophysics 16, 189–214. https://doi.org/10.1016/0040-1951(73)90012-7.

Hudleston, P.J., 1986. Extracting information from folds in rocks. J. Geol. Educ. 34, 237–245. https://doi.org/10.5408/0022-1368-34.4.237.

Hudleston, P.J., Lan, L., 1993. Information from fold shapes. J. Struct. Geol. 15, 253–264. https://doi.org/10.1016/0191-8141(93)90124-S.

Hudleston, P.J., Treagus, S.H., 2010. Information from folds: a review. J. Struct. Geol. 32, 2042–2071. https://doi.org/10.1016/j.jsg.2010.08.011.

Kobberger, G., Zulauf, G., 1995. Experimental folding and boudinage under pure constrictional conditions. J. Struct. Geol. 17, 1055–1063. https://doi.org/10.1016/0191-8141(94)00130-R.

Li, Z., Zeng, Z., Liu, Y., 2023. Boudinage and the rheology of syntectonic migmatites in the highstrain Taili deformation zone, NE China. Geosphere 19, 75–99. https://doi.org/10.1130/GES02523.1.

Lim, C., Cho, M., 2012. Two-phase contractional deformation of the Jurassic Daebo Orogeny, Chungnam basin, Korea, and its correlation with the early Yanshanian movement of China. Tectonics 31, TC1004. https://doi.org/10.1029/2011TC002909.

Mandal, N., Dhar, R., Misra, S., Chakraborty, C., 2007. Use of boudinaged rigid objects as a strain gauge: Insights from analogue and numerical models. J. Struct. Geol. 29 (5), 759–773. https://doi.org/10.1016/j.jsg.2007.02.007Marques.

Marques, F.G., Cobbold, P.R., 1995. Development of highly non-cylindrical folds around rigid ellipsoidal inclusions in bulk simple shear regimes: natural examples and experimental modelling. J. Struct. Geol. 17, 589–602. https://doi.org/10.1016/0191-8141(94)00081-A.

Marques, F.O., Burg, J.-P., Lechmann, S.M., Schmalholz, S.M., 2010. Fluid-assisted particulate flow of turbidites at very low temperature: a key to tight folding in a submarine Variscan foreland basin of SW Europe. Tectonics 29, TC2005. https://doi.org/10.1029/2008TC002439.

Marques, F.O., Fonseca, P.D., Lechmann, S., Burg, J.-P., Marques, A.S., Andrade, A.J.M., Alves, C., 2012. Boudinage in nature and experiment. Tectonophysics 526–529, 88–96. https://doi.org/10.1016/j.tecto.2011.08.017.

Marques, F.O., Mandal, N., 2016. Post-buckling relaxation of an elastic layer and its geological relevance: insights from analogue experiments in pure shear. Tectonophysics 668–669, 82–91. https://doi.org/10.1016/j.tecto.2015.12.004.

Marques, F.O., Podladchikov, Y.Y., 2009. A thin elastic core can control large-scale patterns of lithosphere shortening. Earth Planet Sci. Lett. 277, 80–85. https://doi.org/10.1016/j.epsl.2008.10.009.

Mukherjee, S., 2020. Atlas of Structural Geology. Elsevier. https://doi.org/10.1016/C2018-0-00941-X.

Mynatt, I., Bergbauer, S., Pollard, D.D., 2007. Using differential geometry to describe 3-D folds. J. Struct. Geol. 29, 1256–1266. https://doi.org/10.1016/j.jsg.2007.02.006.

Nabavi, S.T., Fossen, H., 2021. Fold geometry and folding – a review. Earth Sci. Rev. 222, 103812 https://doi.org/10.1016/j.earscirev.2021.103812.

Papeschi, S., Vannucchi, P., Hirose, T., Okazaki, K., 2022. Deformation and material transfer in a fossil subduction channel: evidence from the island of Elba (Italy). Tectonics 41, e2021TC007164. https://doi.org/10.1029/2021TC007164.

Paterson, M.S., Weiss, L.E., 1968. Folding and boudinage of quartz-Rich layers in experimentally deformed Phyllite. Geol. Soc. Am. Bull. 79, 795–812. https://doi.org/10.1130/0016-7606(1968)79[795:FABOQL]2.0.CO;2.

Price, N.J., 1967. The initiation and development of asymmetrical buckle folds in non-metamorphosed competent sediments. Tectonophysics 4, 173–201. https://doi.org/10.1016/0040-1951(67)90051-0.

Ramberg, H., 1955. Natural and experimental boudinage and pinch-and-swell structures. J. Geol. 63, 512–526. https://www.jstor.org/stable/30080904.

Ramberg, H., 1959. Evolution of ptygmatic folding. Nor. Geol. Tidsskr. 39, 99–152.

Ramberg, H., 1981. Gravity, Deformation and the Earth's Crust. Academic Press, London, pp. 1–452.

Ramsay, J.G., 1974. Development of Chevron folds. Geol. Soc. Am. Bull. 85 (11), 1741–1754. https://doi.org/10.1130/0016-7606(1974)85<1741:DOCF>2.0.CO;2.

Ramsay, J.G., Huber, M.I., 1987. The Techniques of Modern Structural Geology – Volume2: Folds and Fractures. Academic press, London, pp. 309–700.

Rast, N., 1956. The origin and significance of boudinage. Geol. Mag. 93, 401–408. https://doi.org/10.1017/S001675680006684X.

Reber, J.E., Schmalholz, S.M., Burg, J.-P., 2010. Stress orientation and fracturing during three-dimensional buckling: numerical simulation and application to chocolate-tablet structures in folded turbidites, SW Portugal. Tectonophysics 493, 187–195. https://doi.org/10.1016/j.tecto.2010.07.016.

Scharf, A., Callegari, I., Mattern, F., Scharf, K., Carminati, E., 2021. Triple folded surface morphology of Neoproterozoic rocks (Jabal Akhdar Dome, Oman Mountains) – Insights into buttressing effects and regional tectonics. J. Asian Earth Sci. 221, 104942 https://doi.org/10.1016/j.jseaes.2021.104942.

Schmalholz, S.M., 2006a. Scaled amplification equation: a key to the folding history of buckled viscous single-layers. Tectonophysics 419, 41–53. https://doi.org/10.1016/j.tecto.2006.03.008.

Schmalholz, S.M., 2006b. Finite amplitude folding of single layers: Elastica, bifurcation and structural softening. Phil. Mag. 86, 3393–3407. https://doi.org/10.1080/14786430500197785.

Schmalholz, S.M., 2008. 3D numerical modeling of forward folding and reverse unfolding of a viscous single-layer: implications for the formation of folds and fold patterns. Tectonophysics 446, 31–41. https://doi.org/10.1016/j.tecto.2007.09.005.

Schmalholz, S.M., Mancktelow, N.S., 2016. Folding and necking across the scales: a review of theoretical and experimental results and their applications. Solid Earth 7, 1417–1465. https://doi.org/10.5194/se-7-1417-2016.

Schmalholz, S.M., Schmid, D.W., Fletcher, R.C., 2008. Evolution of pinch-and-swell structures in a power-law layer. J. Struct. Geol. 30, 649–663. https://doi.org/10.1016/j.jsg.2008.01.002.

Schmid, D.W., Dabrowski, M., Krotkiewski, M., 2008. Evolution of large amplitude 3D fold patterns: a FEM study. Phys. Earth Planet. In. 171, 400–408. https://doi.org/10.1016/j.pepi.2008.08.007.

Schöpfer, M.P.J., Zulauf, G., 2002. Strain-dependent rheology and the memory of plasticine. Tectonophysics 354, 85–99. https://doi.org/10.1016/S0040-1951(02)00292-5.

Sengupta, S., 1983. Folding of boudinaged layers. J. Struct. Geol. 5, 197–210. https://doi.org/10.1016/0191-8141(83)90044-5.

Shaanan, U., Rosenbaum, G., Li, P., Vasconcelos, P., 2014. Structural evolution of the early Permian Nambucca Block (new England orogen, eastern Australia) and implications for oroclinal bending. Tectonics 33, 1425–1443. https://doi.org/10.1002/2013TC003426.

Smith, R.B., 1975. Unified theory of the onset of folding, boudinage, and mullion structure. Geol. Soc. Am. Bull. 86, 1601–1609. https://doi.org/10.1130/0016-7606(1975)86<1601:UTOTOO>2.0.CO;2.

Smith, R.B., 1977. Formation of folds, boudinage, and mullions in non-Newtonian materials. Geol. Soc. Am. Bull. 88, 312–320. https://doi.org/10.1130/0016-7606(1977)88<312:FOFBAM>2.0.CO;2.

Smith, R.B., 1979. The folding of a strongly non-Newtonian layer. Am. J. Sci. 279 (3), 272–287. https://doi.org/10.2475/ajs.279.3.272.

Strömgård, K.-E., 1973. Stress distribution during formation of boudinage and pressure shadows. Tectonophysics 16 (3–4), 215–248. https://doi.org/10.1016/0040-1951(73)90013-9.

Talbot, C.J., Jackson, M.P.A., 1987. Internal kinematics of salt Diapirs. Am. Assoc. Petrol. Geol. Bull. 71, 1068–1093. https://doi.org/10.1306/703c7df9-1707-11d7-8645000102c1865d.

Thiessen, R.L., Means, W.D., 1980. Classification of fold interference patterns: a reexamination. J. Struct. Geol. 2 (3), 311–316. https://doi.org/10.1016/0191-8141(80)90019-X.

Treagus, J.E., Treagus, S.H., 1981. Folds and the strain ellipsoid: a general model. J. Struct. Geol. 3, 1–17. https://doi.org/10.1016/0191-8141(81)90052-3.

Treagus, S.H., 1973. Buckling stability of a viscous single-layer system, oblique to the principal compression. Tectonophysics 19, 271–289. https://doi.org/10.1016/0040-1951(73)90022-X.

Watkinson, A.J., 1975. Multilayer folds initiated in bulk plane strain, with the axis of no change perpendicular to the layering. Tectonophysics 28, T7–T11. https://doi.org/10.1016/0040-1951(75)90030-X.

Watkinson, A.J., 1976. Fold propagation and interference in a single multilayer unit. Tectonophysics 34, T37–T42. https://doi.org/10.1016/0040-1951(76)90092-5.

Weijermars, R., 1997. Principles of Rock Mechanics. Alboran Science Publishing Ltd, pp. 1–360.

Weijermars, R., Schmeling, H., 1986. Scaling of Newtonian and non-Newtonian fluid dynamics without inertia for quantitative modelling of rock flow due to gravity (including the concept of rheological similarity). Phys. Earth Planet. In. 43, 316–330. https://doi.org/10.1016/0031-9201(86)90021-X.

Zawaski, M.J., Kelly, N.M., Orlandini, O.F., Nichols, C.I.O., Allwood, A.C., Mojzsis, S.J., 2020. Reappraisal of purported ca. 3.7 Ga stromatolites from the Isua Supracrustal Belt (West Greenland) from detailed chemical and structural analysis. Earth Planet Sci. Lett. 545, 116409 https://doi.org/10.1016/j.epsl.2020.116409.

Zulauf, G., 1997. Constriction due to subduction: evidence for slab pull in the Mariánské Láznë complex (central European Variscides). Terra. Nova 9, 232–236. https://doi.org/10.1111/j.1365-3121.1997.tb00019.x.

Zulauf, G., Kowalczyk, G., Krahl, J., Petschick, R., Schwanz, S., 2002. The tectonometamorphic evolution of high-pressure low-temperature metamorphic rocks of eastern Crete, Greece: Constraints from microfabrics, strain, illite crystallinity and paleodifferential stress. J. Struct. Geol. 24, 1805–1828. https://doi.org/10.1016/S0191-8141(01)00168-7.

Zulauf, G., Gutiérrez-Alonso, G., Kraus, R., Petschick, R., Potel, S., 2011. Formation of chocolate-tablet boudins in a foreland fold and thrust belt: a case study from the external Variscides (Almograve, Portugal). J. Struct. Geol. 33, 639–1649. https://doi.org/10.1016/j.jsg.2011.08.009.

Zulauf, G., Zulauf, J., Bornemann, O., Kihm, N., Peinl, M., Zanella, F., 2009. Experimental deformation of a single-layer anhydrite in halite matrix under bulk constriction. Part 1: geometric and kinematic aspects. J. Struct. Geol. 31, 460–474. https://doi.org/10.1016/j.jsg.2009.01.013.

Zulauf, G., Zulauf, J., Hastreiter, P., Tomandl, B., 2003. A deformation apparatus for three-dimensional coaxial deformation and its application to rheologically stratified analogue material. J. Struct. Geol. 25, 469–480. https://doi.org/10.1016/S0191-8141(02)00023-8.

Zulauf, G., Zulauf, J., Hattingen, E., 2021. From parasitic via non-cylindrical to extension-parallel folding of oblique single layers under coaxial plane strain: layer rotation around the shortening axis (Z). J. Struct. Geol. 145, 104303 https://doi.org/10.1016/j.jsg.2021.104303.

Zulauf, G., Zulauf, J., Maul, H., 2017. Quantification of the geometrical parameters of non-cylindrical folds. J. Struct. Geol. 100, 120–129. https://doi.org/10.1016/j.jsg.2017.06.001.

Zulauf, J., Zulauf, G., 2004. Rheology of plasticine used as rock analogue: the impact of temperature, composition and strain. J. Struct. Geol. 26, 725–737. https://doi.org/10.1016/j.jsg.2003.07.005.

Zulauf, J., Zulauf, G., 2005. Coeval folding and boudinage in four dimensions. J. Struct. Geol. 27, 1061–1068. https://doi.org/10.1016/j.jsg.2005.04.003.

Zulauf, J., Zulauf, G., Göttlich, J., Peinl, M., 2014. Formation of chocolate-tablet boudins: results from scaled analogue models. J. Struct. Geol. 68, 97–111. https://doi.org/10.1016/j.jsg.2014.09.005.

Zulauf, J., Zulauf, G., Hattingen, E., 2020a. Boudinage and two-stage folding of oblique single layers under coaxial plane strain: layer rotation around the axis of no change (Y). J. Struct. Geol. 135, 104023 https://doi.org/10.1016/j.jsg.2020.104023.

Zulauf, J., Zulauf, G., Hattingen, E., 2020b. Coeval boudinage and folding of oblique single layers under coaxial plane strain: layer rotation around the principal stretching axis (X). J. Struct. Geol. 141, 104217 https://doi.org/10.1016/j.jsg.2020.104217.

Zulauf, J., Zulauf, G., Hattingen, E., 2023. Formation of mullions in two and three dimensions: results from analogue modelling. J. Struct. Geol. 172, 104890 https://doi.org/10.1016/j.jsg.2023.104890.

Zulauf, J., Zulauf, G., Zanella, F., 2016. Formation of dome and basin structures: results from scaled experiments using non-linear rock analogues. J. Struct. Geol. 90, 1–14. https://doi.org/10.1016/j.jsg.2016.07.001.